JM PAPERS

Scaling analysis and self-similarity near breakup of elasto-viscoplastic liquid threads under creeping flow

Pourya Zakeri[1] ⓘ, Pantelis Moschopoulos[1] ⓘ, Yiannis Dimakopoulos[1] ⓘ and John Tsamopoulos[1] ⓘ

[1]Laboratory of Fluid Mechanics and Rheology, Department of Chemical Engineering, University of Patras, Patras 26504, Greece
Corresponding author: John Tsamopoulos, tsamo@chemeng.upatras.gr

We investigate theoretically the breakup dynamics of an elasto-visco-plastic filament surrounded by an inert gas. The filament is initially placed between two coaxial disks, and the upper disk is suddenly pulled away, inducing deformation due to both constant stretching and capillary forces. We model the rheological response of the material with the Saramito–Herschel–Bulkley (SHB) model. Assuming axial symmetry, the mass and momentum balance equations, along with the constitutive equation, are solved using the finite element framework PEGAFEM-V, enhanced with adaptive mesh refinement with an underlying elliptic mesh generation algorithm. As the minimum radius decreases, the breakup dynamics accelerates significantly. We demonstrate that the evolution of the minimum radius, velocity and axial stress follow a power-law scaling, with the corresponding exponent depending on the SHB shear-thinning parameter, n. The scaling exponents obtained from our axisymmetric simulations under creeping flow are verified through asymptotic analysis of the slender filament equations. Our findings reveal three distinct breakup regimes: (*a*) elasto-plastic, (*b*) elasto-plasto-capillary, both with finite-time breakup for $n < 1$, and (*c*) elasto-plasto-capillary with no finite-time breakup for $n = 1$. We show that self-similar solutions close to filament breakup can be achieved by appropriate rescaling of length, velocity and stress. Notably, the effect of the yield stress becomes negligible in the late stages of breakup due to the local dominance of high elastic stresses. Moreover, the scaling exponents are independent of elasticity, resembling the breakup behaviour of finite extensible viscoelastic materials.

Key words: liquid bridges, computational methods, viscoelasticity

1. Introduction

Yield stress (YS) fluids are a class of complex materials that exhibit dual behaviour depending on the magnitude of applied stress. When this magnitude is below a certain threshold they behave like solids, but when it exceeds this threshold, they deform like liquids. This critical threshold is known as the YS (Frigaard 2019). The boundary separating the solid and fluid regions is referred to as the yield surface. The yield surface becomes particularly significant in free-surface flows, and its accurate determination is essential in several scenarios. For example, during the pinch-off of a viscoplastic filament it influences both the final filament shape and the precise location of the pinch point (Moschopoulos *et al.* 2020). Moreover, in the flow of a YS fluid down an inclined plate it governs the evolution of the free surface, and its final shape (Chambon *et al.* 2020), while in the viscoplastic dam break set-up it determines the final arrested interface shape (Liu *et al.* 2016). Understanding the flow characteristics of YS materials is crucial, because they are encountered in nature, as in lava and wet avalanches (Freydier, Chambon & Naaim 2017), and in personal care, cosmetics, food, building, oil and other industries, with products like shaving cream (Huisman, Friedman & Taborek 2012), toothpaste, ice cream, mayonnaise (Ma & Barbosa-Cánovas, 1995), fresh concrete and crude oil (Dimitriou & McKinley 2014). Several models have been developed to describe the transition from solid-like to fluid-like behaviour. The first such model was the Bingham model, which is a generalised Newtonian fluid model with constant viscosity upon yielding. Later, to account for material shear thinning, the Herschel–Bulkley model was introduced (Frigaard 2019). Despite their relative simplicity, these two models require computationally expensive algorithms to accurately resolve regions where the magnitude of the strain-rate tensor approaches zero (Moschopoulos *et al.* 2022), otherwise they require a regularisation parameter to avoid the stress singularity developing as the yield surface is approached.

Over the past two decades, several experimental studies have attempted to clarify the behaviour of YS materials using Carbopol (Putz *et al.* 2008; Niedzwiedz *et al.* 2009; Freydier *et al.* 2017; Luu, Philippe & Chambon 2017), an anionic, high molecular weight polymer composed of acrylic acid cross-linked with an ether, which is transparent, making it more appropriate for experimental observations and measurements. Other experimental studies with YS materials have observed distinct patterns, which are characteristic of viscoelastic fluids, such as the inverted teardrop shape of a rising bubble (Mougin, Magnin & Piau 2012) or the generation of a negative wake by a sedimenting sphere (Putz *et al.* 2008; Holenberg *et al.* 2012). To capture theoretically these observations, an elastic component had to be incorporated into the two original YS fluid models by Saramito (2007, 2009). These new models, known as elasto-visco-plastic (EVP) models, have been used to successfully explain the above-mentioned observations and several others. For example, Fraggedakis, Dimakopoulos & Tsamopoulos (2016) successfully captured the negative wake and the loss of fore-and-aft symmetry in a sedimenting spherical particle in Carbopol. Moreover, Moschopoulos *et al.* (2021) and Kordalis, Dimakopoulos & Tsamopoulos (2024) captured the teardrop shape during the rise of a single or a pair of bubbles in strain-rate-thinning EVP fluids. More recently, Esposito, Dimakopoulos & Tsamopoulos (2024) studied a buoyancy driven motion of a drop in an EVP material.

The buoyancy-driven motions mentioned above involve mixed, shear and elongation flows. To better isolate and control extensional flow, Varchanis *et al.* (2020*a*) studied experimentally the flow of a Pluronic aqueous solution (another EVP fluid) in the optimised shape cross-slot extensional rheometer, conducted simulations using Saramito's model (Saramito 2009) and obtained excellent agreement between experiments and simulations. Filament stretching is another procedure to create a flow field dominated

by extension. The way the filament deforms, and breaks is of paramount importance for many industrial processes, such as coating flows, food processing, spraying of pesticides, direct ink-jet printing and additive manufacturing. In all of them, EVP fluids may be involved (Van Der Kolk, Tieman & Jalaal 2023). The easiest way to isolate such a configuration is to place a small amount of material between two coaxial disks of equal radius and pull the upper disk vertically upward. The material elongates, thins and, finally, pinches off primarily driven by capillarity. To probe the filament stretching dynamics, especially when very short relaxation times need to be measured, several instruments have been developed, like the capillary breakup extensional rheometer (Arnolds *et al.* 2010) (CaBER), the Rayleigh Ohnesorge jetting extensional rheometer (Keshavarz *et al.* 2015) and dripping onto substrate (Rosello *et al.* 2019). The process of filament stretching may be separated into the initial or bulk dynamics and the final or pinching dynamics. In the following we will briefly review the literature that is related either to filament stretching of non-Newtonian, and particularly YS fluids, or to the pinching dynamics.

Filament breakup has been studied with Newtonian (Zhang, Padgett & Basaran 1996) and generalised Newtonian fluids (Yildirim & Basaran 2001) . In both types of materials, a short neck is formed, and the filament breaks in finite time. Viscoelastic materials have been studied quite extensively and early on under extensional flow (McKinley & Sridhar 2002), due to their widespread use and importance in practical applications, as well as the intriguing phenomena that arise. When a viscoelastic filament thins, strong tensile stresses develop that oppose the necking of the fluid thread. This increases the lifetime of the bridge and leads to the formation of a quite longer and cylindrical thread that connects the two drops that remain in contact with the corresponding disk (Clasen *et al.* 2006). Under specific material properties and in the presence of elastic and inertia effects a small satellite drop may develop in the middle of the filament (Bhat *et al.* 2010; Varchanis *et al.* 2018).

Turning our attention to filaments of YS materials, initially Martinie, Buggisch & Willenbacher (2013), and Niedzwiedz, Buggisch & Willenbacher (2010) tried to measure the so-called extensional YS using the CaBER. However, their measurements did not agree with the ideal viscoplastic theory that predicted the extensional YS to be $\sqrt{3}$ times the shear YS. This deviation was caused because the elastic stresses in the von Mises criterion were neglected (Varchanis *et al.* 2020*a*). Furthermore, Balmforth, Dubash & Slim (2010*a*) investigated the primarily extensional flow taking place in drips and bridges of different YS materials and compared their experimental results with the viscoplastic slender theory they developed. Then, they used this theory to study the pinching dynamics of YS materials (Balmforth, Dubash & Slim 2010*b*). Interestingly, they showed that, just before pinching, the breakup dynamics became universal, and was dictated by a simple power law, the exponent of which coincided with the exponent of power-law fluids (Doshi *et al.* 2003; Suryo & Basaran 2006), and that the YS had almost no effect on the scaling law. On the other hand, Huisman *et al.* (2012) and Niedzwiedz *et al.* (2010) observed experimentally that, although YS stress materials followed the scaling laws of shear-thinning materials, they also formed a longer cylindrical neck connecting the upper and lower conical parts of the bridge, without examining whether the material in the bridge actually exhibited elastic properties. More recently, Moschopoulos *et al.* (2020) performed two-dimensional simulations assuming axial symmetry of the bulk and pinching dynamics of a thread with viscoplastic properties. Thus, they confirmed the above-mentioned scaling laws for viscoplastic materials (Balmforth *et al.* 2010*b*). However, their simulations did not capture the cylindrical neck that had been experimentally observed, (Niedzwiedz *et al.* 2010). This shortcoming was alleviated by Moschopoulos *et al.* (2023), when they included material elasticity by using the Saramito–Herschel–Bulkley model and predicted the formation of a long and slender neck that connected the upper and lower parts of the Carbopol filament

undergoing stretching. Nevertheless, they did not investigate the pinching dynamics in detail and whether it is governed by similarity solutions. Such analysis has been developed for Newtonian, viscoplastic and viscoelastic materials.

Understanding the underlying physics during pinching (Tuladhar & Mackley 2008; Townsend *et al.* 2019; Van Der Kolk *et al.* 2023) is crucial for advancing industrial tools, notably those used in inkjet or 3D printing, for controlling the droplet size, which may be created after filament breakup or reducing food residuals during the filling process in designing production lines. While stretching the fluid thread, the mass conservation and capillarity on its free surface shrink the filament radius to zero somewhere along the filament. At this location and time instant the governing equations become singular. Thus, stress and velocity diverge, making the dynamics independent of the boundary conditions governing the earlier bulk dynamics. Hence, the local dynamics in the abruptly thinning filament will exhibit universality, and self-similarity could be achieved at the vicinity of the singular point. This idea of universality was proposed first by Keller & Miksis (1983), assuming potential flow in the filament. Since then, various authors have described the pinch-off dynamics of Newtonian liquids (Eggers 1993; Eggers & Dupont 1994; Papageorgiou 1995; Brenner, Lister & Stone 1996; Chen, Notz & Basaran 2002), with or without inertia. Concerning complex fluids, numerous studies have been conducted following and extending the ideas for Newtonian liquids to describe pinching when the rheological model of the filament is a power law (Doshi *et al.* 2003; Renardy & Renardy 2004; Suryo & Basaran 2006), viscoelastic (Bechtel, Cao & Forest 1992; Anna & McKinley 2001; Renardy 2002*b*; Fontelos & Li 2004; Clasen *et al.* 2006; Turkoz *et al.* 2018) or viscoplastic (Balmforth *et al.* 2010*b*; Moschopoulos *et al.* 2020).

However, efforts to describe the bulk and pinch-off dynamics of a bridge composed of an EVP material are very limited. We are aware only of the work by Moschopoulos *et al.* (2023), who studied the bulk dynamics thoroughly and filament thinning only to some extent but did not examine the asymptotics or self-similarity close to breakup. The present study aims to fill this gap by determining the breakup asymptotics, the existence of self-similar solutions by employing two-dimensional (2-D) axisymmetric simulations coupled with a sharp interface tracking method, while fluid inertia is neglected.

The paper is organised as follows: in § 2, the problem formulation is presented, the equations and boundary conditions governing the axisymmetric flow are introduced, followed by the slender filament (1-D) equations. In § 3, we very briefly review the solution method, postponing to Appendix A certain important techniques about mesh generation, refinement, restructuring and variable interpolation between different meshes. We dedicate § 4 to extracting asymptotic pinch-off scales from the slender filament equations. In the same section we include the approximate solution under the assumption that the filament undergoes a strictly uniaxial extension. In § 5, we present our 2-D results concerning filament pinching, self-similar solutions,- and we conduct a parametric study. Finally, we summarise our findings in § 6.

2. Problem formulation

2.1. *General two-dimensional formulation*

In what follows, variables or parameters with tilde (˜) over them, are denoted as dimensional while their dimensionless counterparts are presented without tilde. We consider a 2-D, axisymmetric liquid bridge of an EVP material held captive between two parallel and coaxial disks. The initial separation of the two disks is $\tilde{L}_0$ and their common radius is $\tilde{h}_0$, both of which are of the order of a few millimetres, at the most, making
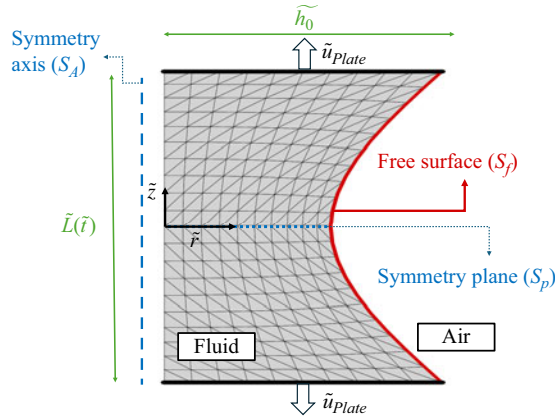
Figure 1. Schematic of the axisymmetric EVP filament stretching geometry.

gravitational effects very small from the beginning of the process. The material is pinned to the disk's perimeter, so that the initial radius of the fluid thread is also $\tilde{h}_0$. At time $\tilde{t} = 0^+$, the upper plate starts to move with constant velocity in the positive $\tilde{z}$-direction. As time proceeds, the capillary force and material stress components start to grow, and a neck is formed in the filament. We monitor the time evolution of the minimum radius of the filament as it shrinks to zero, $\tilde{h}_{min} \to 0$, along with the dominant velocity and stress components. The negligible gravity force allows us to assume a symmetry plane at $\tilde{z} = 0$, making it possible to simulate only the top half of the filament. Figure 1 shows a schematic of the axisymmetric EVP bridge being stretched with symmetry plane imposed at $\tilde{z} = 0$.

The characteristic scales used for making the variables dimensionless are those proposed by Moschopoulos *et al.* (2023) for the bulk dynamics of an EVP filament stretching. The radius of the disk $\tilde{h}_0$ and the capillary force ($\tilde{\sigma}/\tilde{h}_0$), scale all lengths and pressure or stress components, respectively. Balancing capillarity and viscous stresses results in the visco-capillary time, which is used as the characteristic time scale, $\tilde{t}_{vc} = (\tilde{k}\tilde{h}_0/\tilde{\sigma})^{(1/n)}$, where $\tilde{k}$ (Pa s^n) is the consistency index, and n is the shear-thinning exponent of the Saramito–Herschel–Bulkley (SHB) model. The velocity scale is $\tilde{h}_0/\tilde{t}_{vc}$. Another form of stress scale, equivalent to the one given earlier, is $\tilde{k}/(\tilde{t}_{vc})^n$. Introducing these characteristic scales in the governing equations results in the dimensionless numbers for the present analysis, which are given in table 1.

With these characteristic quantities, the dimensionless mass and momentum conservation equations become

$$Oh^{-2} \frac{D\boldsymbol{u}}{Dt} = -\nabla p + \nabla \cdot \boldsymbol{\tau} + \nabla \cdot \boldsymbol{\tau}_s - Bo \, \boldsymbol{e}_z, \tag{2.1}$$

$$\nabla \cdot \boldsymbol{u} = 0, \tag{2.2}$$

where D/Dt is the substantial derivative, $\boldsymbol{u}$ the velocity vector, ∇ the gradient operator, $\boldsymbol{\tau}_s$ the Newtonian solvent stress, $\boldsymbol{\tau}$ the polymeric extra stress tensor, p the pressure and $\boldsymbol{e}_z$ the unit vector in the positive z-direction. In this study, the Newtonian solvent contribution is taken to be zero, hence $\boldsymbol{\tau}_s = \boldsymbol{0}$. Furthermore, in this study we will neglect inertial effects, setting $Oh^{-2} = 0$. The polymeric extra stress tensor is described by the SHB (Saramito 2009) EVP model for the rheological response of the material

$$Ec \overset{\nabla}{\boldsymbol{\tau}} + \max(0, |\boldsymbol{\tau}_d| - Y_s)^{\frac{1}{n}} \frac{\boldsymbol{\tau}}{|\boldsymbol{\tau}_d|} = \dot{\boldsymbol{\gamma}}. \tag{2.3}$$

Definition	Name	Physical interpretation
$Oh = \dfrac{\bar{k}^{\frac{1}{n}}}{\sqrt{\tilde{\rho}\tilde{h}_0^{\left(3-\frac{2}{n}\right)}\tilde{\sigma}^{\left(\frac{2}{n}-1\right)}}}$	Ohnesorge number	Ratio of viscous forces to combined inertia and surface tension forces. The parameter Oh^{-2} is often called the capillary Reynolds number, because it uses the visco-capillary scale for velocity.
$Y_s = \dfrac{\tilde{\tau}_y\tilde{h}_0}{\tilde{\sigma}}$	Dimensionless YS	Ratio of YS to capillarity.
$Bo = \dfrac{\tilde{\rho}\tilde{g}\tilde{h}_0^2}{\tilde{\sigma}}$	Bond number	Ratio between gravitational and surface tension (capillary) forces. With $\tilde{h}_0$ up to a mm, Bo is up to 0.1, making the gravitational force negligible.
$Ec = \dfrac{\tilde{\sigma}}{\tilde{G}\tilde{h}_0}$	Elasto-capillary number	Ratio of surface tension force to elastic modulus. Higher Ec leads to more pronounced elastic stresses.
$V = \dfrac{\tilde{V}}{\tilde{h}_0^3}$	Dimensionless bridge volume	Scales the volume of the material held between the two plates with plate radius.
$L = \dfrac{\tilde{L}}{\tilde{h}_0}$	Bridge aspect ratio	Scales the height of the bridge in the direction of stretching with the plate radius.

Table 1. Dimensionless numbers.

The first term in this model is the elastic contribution and the second one is the viscoplastic contribution to the total rate of deformation tensor, $\dot{\boldsymbol{\gamma}} = \nabla\boldsymbol{u} + (\nabla\boldsymbol{u})^T$. In the above model, $\overset{\nabla}{\boldsymbol{\tau}}$ is the upper-convected derivative of extra stress tensor, which is defined as

$$\overset{\nabla}{\boldsymbol{\tau}} = \frac{\partial\boldsymbol{\tau}}{\partial t} + \boldsymbol{u}\cdot\nabla\boldsymbol{\tau} - (\nabla\boldsymbol{u})^T\cdot\boldsymbol{\tau} - \boldsymbol{\tau}\cdot\nabla\boldsymbol{u}. \tag{2.4}$$

Also, $\boldsymbol{\tau}_d = \boldsymbol{\tau} - (tr(\boldsymbol{\tau})/tr(\boldsymbol{I}))$ is the deviatoric part of extra stress tensor with magnitude $|\boldsymbol{\tau}_d| = \sqrt{(1/2)\boldsymbol{\tau}_d : \boldsymbol{\tau}_d}$, and $(\nabla\boldsymbol{u})^T$ indicates the transpose of the velocity gradient. The max term determines the transition from a solid-like to a fluid-like region by incorporating the von Mises criterion. If $|\boldsymbol{\tau}_d|$ exceeds Y_s, the material yields and deforms like a viscoelastic fluid with shear thinning, otherwise it behaves like a neo-Hookean solid. The free surface of the filament, S_f, is in contact with air, which is assumed to have negligible viscosity and density. In our formulation, nodes on S_f are treated in a Lagrangian sense, hence the velocity of the mesh and the velocity of the fluid particle on S_f in the direction normal to S_f must be equal. This is the so-called kinematic boundary condition and serves as a boundary condition on the free surface. Furthermore, the total stress from the fluid side acting on S_f must balance capillarity, given that air is dynamically inert. This is the so-called traction boundary condition. These two boundary conditions are

$$\boldsymbol{n}\cdot(\boldsymbol{u} - \boldsymbol{u}_m) = 0, \quad on\ S_f, \tag{2.5}$$
$$\boldsymbol{n}\cdot\boldsymbol{T} = (2\mathcal{H})\,\boldsymbol{n}, \quad on\ S_f, \tag{2.6}$$

where $\boldsymbol{u}_m$ is the velocity of the mesh nodes and $\boldsymbol{n}$ the outward unit vector normal to S_f; $\boldsymbol{T}$ the total stress tensor, defined as $\boldsymbol{T} = -p\boldsymbol{I} + \boldsymbol{\tau}$, with $\boldsymbol{I}$ the unit tensor;

1020 A37-6

$2\mathcal{H} = -\nabla_s \cdot \boldsymbol{n}$ is twice the mean curvature of S_f and lastly $\nabla_s = (\boldsymbol{I} - \boldsymbol{nn}) \cdot \nabla$ is the surface gradient operator (Deen 2012). We have assumed axial symmetry with axis at $r = 0$, or on S_A and planar symmetry at $z = 0$, or on S_p. On these boundaries the no-shear and no-penetration boundary conditions are applied

$$\boldsymbol{n} \cdot \boldsymbol{T} \cdot \boldsymbol{t} = 0, \quad \text{on } S_A \text{ and } S_P, \tag{2.7}$$

$$\boldsymbol{n} \cdot \boldsymbol{u} = 0, \quad \text{on } S_A \text{ and } S_P, \tag{2.8}$$

where $\boldsymbol{t}$ is the unit vector tangential to either S_A or S_p. The fluid in contact with the two solid disks, initially at rest, follows the no-slip and no-penetration boundary conditions and when $t > 0$, the upper solid disk starts to move suddenly with dimensionless velocity U

$$\begin{cases} t = 0, & \boldsymbol{u} = 0 \\ t > 0, & \boldsymbol{u} = U\boldsymbol{e}_z \end{cases} \quad \text{at} \quad z = L, \tag{2.9}$$

$$\boldsymbol{u} = \boldsymbol{0}, \quad \text{at} \quad z = 0, \tag{2.10}$$

where $L = L_0 + Ut$ is the disk separation at time t. The contact point on the intersection between the free surface S_f and the solid disks is pinned

$$h_0 = 1, \quad \text{at} \quad z = L \quad \text{and} \quad z = 0. \tag{2.11}$$

Due to the hyperbolic nature of the SHB model (and similarly for most other constitutive laws for polymeric liquids), the boundary conditions for the extra stress tensor are needed only at the inflow (Van Der Zanden & Hulsen 1988). In this problem, no inflow conditions exist, and no stress boundary conditions are required, except for $\boldsymbol{n} \cdot \boldsymbol{T} \cdot \boldsymbol{t} = 0$ at the axis of symmetry and the symmetry plane along with the force balance at the free interface.

2.2. *Slender thread equations*

Assuming that to highest order the variation of all flow variables in the radial direction, r, is negligible compared with that in the axial direction, z (except for u_r, and τ_{rz}, which vary linearly with r), the interface S_f can be described as a function of z alone, S_f, $r = h(z, t)$, disallowing any overturning of the free surface. Then the previously presented 2-Dl equations can be reduced to a much simpler, 1-D equation set. These are the so-called slender filament equations. The reduced mass and momentum equations, still neglecting solvent viscosity, are (Bechtel *et al.* 1992; Clasen *et al.* 2006)

$$\frac{\partial h^2}{\partial t} + \frac{\partial}{\partial z}(u_z h^2) = 0, \tag{2.12}$$

$$Oh^{-2}\left(\frac{\partial u_z}{\partial t} + u_z \frac{\partial u_z}{\partial z}\right) = \frac{\partial}{\partial z}(2\mathcal{H}) + \frac{1}{h^2}\frac{\partial}{\partial z}\left(h^2(\tau_{zz} - \tau_{rr})\right), \tag{2.13}$$

$$2\mathcal{H} = \frac{h_{zz}}{\left(1 + h_z^2\right)^{\frac{3}{2}}} - \frac{1}{h\left(1 + h_z^2\right)^{\frac{1}{2}}}, \tag{2.14}$$

where $u_z(z, t)$ is the axial velocity, $2\mathcal{H}$ is twice the mean curvature of the free surface, now explicitly written in the cylindrical coordinate system and the subscript z next to h, as in h_z, indicates partial differentiation; in this case, $(\partial h/\partial z)$. Please note that in §2.2 all variables have retained their usual symbols but depend only in the axial direction z and time, t. Equation (2.13) is the reduced form of the dominant momentum balance in the axial direction, in which pressure has been eliminated in favour of the curvature term via the normal force balance and the next-order term of the axial velocity has been eliminated via the tangential force balance. As stated in the previous section, we will analyse the slender filament equations ignoring inertia. Although the computational effort to solve the

1-D equations is considerably smaller than the effort to solve their 2-D counterparts, the former equations are not accurate enough to capture the flow field under certain conditions (Suryo & Basaran 2006; Turkoz *et al.* 2018). In this study, we avoid conducting 1-D simulations; we will use the slender filament equations only to derive the asymptotic decay of the radius and growth of the stress in the pinch-off regime.

3. Finite element solution

Our numerical algorithm for solving the 2-D equation set is based on the recently developed Petrov–Galerkin finite element formulation for viscoelastic free-surface flows. This method allows us to use equal-order linear interpolants for all variables, circumventing the requirement for mixed finite element formulations for velocity, pressure and stress to satisfy the Ladyzhenskaya–Babuška–Brezzi conditions, and simultaneously does not suffer from the high Weissenberg number problem. To achieve all these advantages, Varchanis *et al.* (2019*b*) have carefully chosen specific stabilising terms for the weak form of the governing equations. Coupling this method with the quasi-elliptic mesh generator (Dimakopoulos & Tsamopoulos 2003; Chatzidai *et al.* 2009) allows us to obtain stable numerical solutions even in highly deformed meshes and for very high values of fluid elasticity (Varchanis *et al.* 2020*b*). This method has been tested in benchmark flows and many other studies with steady and moving boundary problems, confirming its accuracy and robustness (Moschopoulos *et al.* 2021; Varchanis *et al.* 2021; Kordalis *et al.* 2023; Moschopoulos *et al.* 2024; Kordalis *et al.* 2024)

To solve the set of partial differential equations in this problem, the domain is discretised into elements, altogether forming the mesh. According to Moschopoulos *et al.* (2023), we prefer linear three-node triangular elements to linear quadrangles for their better representation of the free surface. Additionally, we utilise right-angle triangles for mesh construction, as they exhibit better convergence behaviour compared with other types of domain triangulation methods. For accurately tracking the displacement of free surface, we employ the arbitrary Lagrangian Eulerian formulation. In this method the normal displacement of the free surface is dictated by its Lagrangian movement, whereas all other nodes inside the liquid domain are positioned arbitrarily to achieve a smooth mesh for solution accuracy. To optimise the mesh within the domain, we selected the quasi-elliptic grid generation scheme proposed by Dimakopoulos & Tsamopoulos (2003). As suggested in previous studies (Notz & Basaran 2004; Suryo & Basaran 2006; Bhat *et al.* 2010), using a highly non-uniform mesh where elements are densely concentrated in the necking region is essential for accurate and efficient computation of breakup problems. However, even in a densely packed mesh generated by the quasi-elliptic grid generation scheme, the elements will become highly distorted, leading to divergence of the numerical algorithm as $h_{min} \to 0$. To address this issue, we introduce additional nodes on radial cross-sections to maintain the quality of the mesh as breakup is approached. Computational experiments indicate that full domain remeshing introduces significantly larger errors during solution transfer from the previous to the new mesh than simply adding nodes. Therefore, we do not use full domain remeshing. This approach allows us to start computations with a relatively coarse mesh and progressively refine it as $h_{min} \to 0$, while ensuring a smooth mesh and an accurate solution.

For the time integration and iterative scheme to solve the matrix system assembled by the finite element formulation, we employ the same procedure reported by Moschopoulos *et al.* (2023). Convergence of Newton's iterations at each time step is accepted if the Euclidean norm of both the residual and the Newton's correction vector falls below of 10^{-6}. Certain important ideas about mesh refinement and variable interpolation between
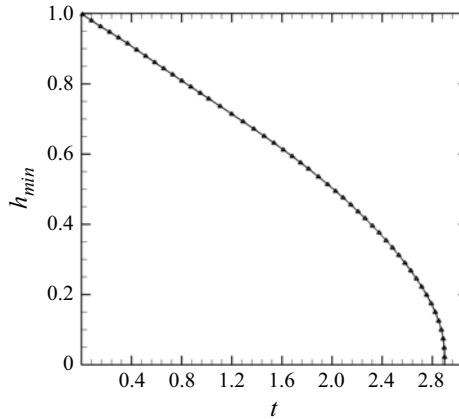
Figure 2. The evolution of minimum radius vs. time, for parameter values
$n = 0.45$, $Ec = 0.14$, $Y_s = 1.25$, $U = 0.39$.

meshes are given in Appendix A. In the supplementary material SM1, we present the evolution of the mesh either for the entire domain, or in the neck where continuous mesh refinement takes place.

4. Asymptotic analysis for an EVP thread

4.1. *Asymptotic analysis near filament pinching at the symmetry plane via the slender thread equations following the SHB model*

Since we are seeking a self-similar solution in the vicinity of the singular point, where $h_{min} \to 0$, we introduce two new local variables, Z and T, which are defined as

$$Z = z - z_0, \tag{4.1}$$
$$T = t_0 - t. \tag{4.2}$$

In the above expressions, Z denotes the axial distance from the singular point (the location of h_{min}), the axial coordinate of which is z_0. Having set $Oh^{-2} = 0$, to neglect inertia in the momentum equation, we find $z_0 = 0$ in all our simulations and z is probed where $h = 1.01 h_{min}$. Here, T is the time until the breakup time, which is denoted as t_0. Preliminary 2-D results indicate that the time evolution of the minimum radius follows the pattern shown in figure 2.

This figure clearly demonstrates that the breakup time of the filament is finite, a trend observed in all our simulations for values of n less than unity. This should have been expected, because the SHB model predicts a finite extensible material, which is known to have a finite breakup time as opposed to the Oldroyd-B fluid, which approaches breakup exponentially (Renardy 1995; McKinley 2005). Hence, we introduce self-similar forms with power-law functions for the axial position, axial velocity and axial component of extra stress tensor

$$h\left(Z, T\right) = T^{\alpha_1} \phi\left(\xi\right), \tag{4.3}$$
$$u_z\left(Z, T\right) = T^{\alpha_2} \psi\left(\xi\right), \tag{4.4}$$
$$\tau_{zz}\left(Z, T\right) = T^{\alpha_3} \Omega\left(\xi\right), \tag{4.5}$$

$$\xi = \frac{Z}{T^\delta}. \tag{4.6}$$

Please note that in §4 all variables have retained their previous symbols but now are functions of Z, T. Moreover, ξ denotes the similarity variable and the exponent δ controls the time dependence of the extent of the similarity region. When the filament radius becomes extremely small, both $u_z(Z, T)$ and $\tau_{zz}(Z, T)$ in the vicinity of the singular point grow increasingly fast. Under these conditions, the nonlinear terms in the EVP constitutive equation become dominant. From now on, we will refer to this regime as the highly nonlinear regime. Next, we substitute the self-similar forms of $h(Z, T)$ and $u_z(Z, T)$, in the continuity equation, (2.12), and enforce time invariance to obtain

$$\delta - \alpha_2 = 1, \quad \phi' = \phi \frac{\alpha_1 - \dfrac{\psi'}{2}}{\psi + \delta\xi}. \tag{4.7}$$

Given that the axial momentum equation is the dominant momentum balance and τ_{zz} the dominant stress component, we analyse the z-component of the constitutive equation, which according to the SHB model is

$$\frac{\partial \tau_{zz}}{\partial t} + u_z \frac{\partial \tau_{zz}}{\partial z} = 2 \frac{\partial u_z}{\partial z} \tau_{zz} + \frac{2}{Ec} \frac{\partial u_z}{\partial z} - \frac{\max(0, \, |\boldsymbol{\tau_d}| - Y_s)^{\frac{1}{n}}}{Ec} \frac{\tau_{zz}}{|\boldsymbol{\tau_d}|}. \tag{4.8}$$

According to its definition, $|\boldsymbol{\tau_d}|$ is

$$|\boldsymbol{\tau_d}| = \sqrt{\frac{1}{2} \left(\left(\tau_{rr} - \frac{tr(\boldsymbol{\tau})}{3} \right)^2 + 2\tau_{rz}^2 + \left(\tau_{zz} - \frac{tr(\boldsymbol{\tau})}{3} \right)^2 + \left(\tau_{\theta\theta} - \frac{tr(\boldsymbol{\tau})}{3} \right)^2 \right)}. \tag{4.9}$$

In regions of high nonlinearity $tr(\boldsymbol{\tau}) \approx \tau_{zz}$, yielding

$$|\boldsymbol{\tau_d}| \approx \sqrt{\left(\frac{1}{2} \right) \left[\left(-\frac{\tau_{zz}}{3} \right)^2 + \left(\frac{2\tau_{zz}}{3} \right)^2 + \left(-\frac{\tau_{zz}}{3} \right)^2 \right]} = \sqrt{\frac{1}{3}\tau_{zz}^2} = \frac{1}{\sqrt{3}} |\tau_{zz}|. \tag{4.10}$$

Moreover, in the same region $|\tau_{zz}| \gg Y_s$, while in the upper half of the thread that we examine $\tau_{zz} \geq 0$, simplifying the max term in the EVP constitutive equation to $(1/\sqrt{3}\tau_{zz})^{1/n}$. Therefore, the YS does not enter the dominant balance in the constitutive law and the entire thread is yielded in all examined cases. By assuming that the normal z-component of the stress tensor in the EVP thread is constant, we neglect the convective part of the substantial derivative in (4.8). The rest of the terms in the EVP constitutive equation are approximated following ideas in Renardy (1995) and Fontelos & Li (2004), resulting in

$$\frac{\partial \tau_{zz}}{\partial t} = 2 \frac{\partial u_z}{\partial z} \tau_{zz} - \frac{\left(\frac{1}{\sqrt{3}} \tau_{zz} \right)^{\frac{1}{n}}}{Ec} \sqrt{3}. \tag{4.11}$$

Substituting the assumed forms for the similarity variables and enforcing time invariance yields

$$\alpha_3 = \frac{n}{n-1}, \quad -\alpha_3 \Omega + \delta\xi\Omega' = 2\phi'\Omega - \frac{1}{Ec\left(\sqrt{3}\right)^{n-1}} \Omega^{\frac{1}{n}}. \tag{4.12}$$

Considering inertialess physics, the slender momentum equation, (2.13), becomes

$$\frac{\partial}{\partial z}\left(h + h^2(\tau_{zz} - \tau_{rr})\right) = 0. \tag{4.13}$$

For this balance to be consistent, τ_{zz} must grow like $1/h$ so we can conclude that

$$\alpha_1 = -\alpha_3 = \frac{n}{1-n}. \tag{4.14}$$

Turning our attention again to the mass conservation equation, we obtain

$$\phi' = \phi \frac{\alpha_1 - \dfrac{\psi'}{2}}{\psi + \delta\xi}. \tag{4.15}$$

The denominator will be zero where $\psi = -\delta\xi$, for $\xi = \xi_0$. Therefore, as in the Newtonian (Doshi *et al.* 2003; Eggers 1993) or the power-law material (Doshi *et al.* 2003), a smooth solution exists only if, at $\xi = \xi_0$, the following hold:

$$\psi\,(\xi_0) = -\delta\xi_0, \tag{4.16}$$
$$\psi'\,(\xi) = 2\alpha_1. \tag{4.17}$$

Hence, a Taylor series expansion in ξ about $\xi = \xi_0$ as in Doshi *et al.* (2003) results in

$$\phi\,(\xi - \xi_0) = \phi_0 + \phi_2\,(\xi - \xi_0)^2 + \phi_4\,(\xi - \xi_0)^4 + \ldots, \tag{4.18}$$
$$\psi\,(\xi - \xi_0) = -\delta\xi_0 + 2\alpha_1\,(\xi - \xi_0) + \psi_3\,(\xi - \xi_0)^3 + \ldots, \tag{4.19}$$

where ϕ_0, ϕ_2, ... and ψ_3, ... are the coefficients of the expansion. In all our simulations, the value of the axial velocity is zero at the plane of symmetry, which arises at $\xi_0 = 0$ for inertialess flow physics. Therefore, ϕ and ψ are even and odd functions, respectively. The minimum value of ϕ is ϕ_0. Hence, the minimum radius takes the following power-law form:

$$h_{min}\,(t) = \phi_0\,T^{\alpha_1}, \tag{4.20}$$

where ϕ_0 depends on physical properties and can be determined numerically. In this study, because of the dual nature of the material, and particularly the max term in the constitutive model, the flow is more complicated, and we do not determine analytically the value of ϕ_0. This could be pursued in future studies. The main focus of this study is the breakup asymptotic forms and the existence of self-similarity. In a nutshell, the results for the scalings in the capillary breakup regime are given by (4.7a) and (4.14).

The asymptotes derived above are similar with those derived by Renardy, (2002a) for a generalised form of the viscoelastic Phan–Thien–Tanner (G-PTT) model. The G-PTT fluid described in Renardy, (2002a) in dimensional form can be written as follows:

$$\lambda \overset{\nabla}{\tilde{\boldsymbol{\tau}}} + \tilde{\boldsymbol{\tau}} + \frac{\nu\tilde{\lambda}^{a-1}}{\tilde{\eta}_p^{a-1}}\,(tr\,(\tilde{\boldsymbol{\tau}}))^{a-1}\,\tilde{\boldsymbol{\tau}} = \tilde{\eta}_p\,\tilde{\dot{\boldsymbol{\gamma}}}, \tag{4.21}$$

where $a > 1$ is the exponent of the G-PTT model, $\tilde{\lambda}$ is the relaxation time, $\tilde{\eta}_p$ is the polymeric viscosity and ν is a positive dimensionless number, playing the same role as the mobility factor in the Giesekus model. The z-component of G-PTT model where τ_{zz} is the dominant stress component is

$$\frac{\partial\tilde{\tau}_{zz}}{\partial\tilde{t}} = 2\frac{\partial\tilde{u}_z}{\partial\tilde{z}}\tilde{\tau}_{zz} - \frac{\nu\tilde{\lambda}^{a-2}}{\tilde{\eta}_p^{a-1}}\tilde{\tau}_{zz}^a. \tag{4.22}$$

Equation (4.22) reduces to (4.11) if the exponent a in (4.22) is replaced by $(1/n)$. Hence, it is expected that the G-PTT model will have the same asymptotes as the SHB model in the breakup regime. According to Renardy, (2002a), the asymptotes of the G-PTT

1020 A37-11

model are

$$\alpha_1 = \frac{1}{a-1}, \quad \alpha_2 = -1, \quad \alpha_3 = \frac{1}{1-a}, \quad \text{if } 1 < a < \frac{7}{3}, \tag{4.23}$$

$$\alpha_1 = \frac{1}{4a-8}, \quad \alpha_2 = -1, \quad \alpha_3 = \frac{1}{1-a}, \quad \text{if } \frac{7}{3} < a < 3. \tag{4.24}$$

For $(7/3) < a < 3$ $(0.33 < n < 0.43)$, surface tension has no influence on breakup, and pinching enters a new regime, the so-called elastic breakup regime. Our numerical results are consistent with this finding, as we will demonstrate in § 5.5.2. Integration of (4.13) yields

$$h + h^2 \tau_{zz} = F(t), \tag{4.25}$$

where $F(t)$ is the total force acting on the filament cross-section. In the elastic breakup regime, the first term on the left-hand side is associated with capillarity and is subdominant. Substituting α_1 and α_3, as given in (4.24), into the asymptotic forms of (4.3) and (4.5), one obtains

$$F(t) \sim h^2 \tau_{zz} \sim (t_0 - t)^{2\alpha_1 + \alpha_3} \sim (t_0 - t)^{\frac{2n - 6n^2}{(n-1)(4-8n)}}. \tag{4.26}$$

For the force to be finite, requires that $(2n - 6n^2)/(n-1)(4-8n) > 0$ which yields $n > 1/3$. Indeed, our code did not converge for values $n < 0.33$. Furthermore, Renardy suggests that $\delta = 0$, $\alpha_2 = -1$, but our 2-D numerical results slightly deviate from this value. The reason for this difference is probably caused by the fact that Renardy has neglected any radial dependence of u_z, p, τ_{zz}, τ_{rr} and $\tau_{\theta\theta}$ and completely neglected u_r, τ_{rz}, which is not entirely correct, as will be seen in § 5. On the other hand, our solution of the 2-D equations may include numerical error. We calculate the following scaling exponents for axial velocity and axial position numerically:

$$\alpha_2 = \frac{n}{n-1} (<0), \quad \delta = \frac{n}{n-1} + 1 (<0), \quad \text{if} \quad n > 0.5, \tag{4.27}$$

where and

$$\alpha_2 \to -1, \delta \to 0, \quad \text{if} \quad n \le 0.5 \quad \text{and} \quad n \to 0.4. \tag{4.28}$$

In late stages of breakup, since τ_{zz} is dominant over τ_{rr}, the asymptotic behaviour of the transient extensional viscosity $\eta_{ext} = (\tau_{zz} - \tau_{rr})/\dot{\epsilon}_{local}$ yields

$$\eta_{ext} \sim (t_0 - t)^{\frac{2n-1}{n-1}}. \tag{4.29}$$

Clearly, for $n > 0.5$, η_{ext} diverges to infinity, while for $n < 0.5$, η_{ext} tends to 0, indicating transient extension-rate-thickening and -thinning behaviours, respectively. It is noteworthy that the exponents in EVP fluids are different from those in power-law or viscoplastic fluids. Similar deviations have been observed in experiments with shear-thinning viscoelastic materials where scalings do not follow expected asymptotes of a power-law material (Moon *et al.* 2024). In all our simulations, the scaling exponent for the axial position, denoted as δ, is found to be negative. We are probing the axial position at z where $h = 1.01 h_{min}$. The negative sign of δ implies that the neck length increases as breakup is approached, instead of decreasing, as is usually the case with $\delta > 0$. Moreover, the magnitude of the scaling exponent of the minimum radius, $|\alpha_1|$, consistently exceeds $|\delta|$ in our simulations. Hence, the thinning of the thread occurs faster than the growth of the length of the neck. Consequently, although breakup still occurs at $z = 0$, the axial extent of fast thinning increases. This has been called 'breakup at a finite axial length' by Renardy,

(2002a) who found that $\delta = 0$, analytically for the G-PTT fluid. This implies that the neck length remains constant. Consequently, the inertialess breakup of EVP fluids occurs over a finite length, whereas in power-law or viscoplastic fluids, it takes place at a single point. These ideas will be discussed and supported further in § 5.5.4.

4.2. *Ideal uniaxial extension of an EVP material under highly nonlinearity conditions*

To further validate the derived scaling exponents for h and τ_{zz}, we solve numerically an ideal uniaxial extension flow with the EVP constitutive equation. This simplification reduces the slender jet equations to those for a perfectly cylindrical liquid jet under extension. Thus, the strain rate becomes

$$\dot{\epsilon} = \frac{\partial u_z}{\partial z} = -\frac{2}{h}\frac{\mathrm{d}h}{\mathrm{d}t}. \tag{4.30}$$

Assuming the power-law asymptote for the radius, the local strain rate reduces to

$$h = \phi_0 (t_0 - t)^{\alpha_1} \implies \dot{\epsilon} = \frac{2\alpha_1}{t_0 - t} \approx \frac{2}{T}. \tag{4.31}$$

We note that assuming $(2\alpha_1)/(t_0 - t) \approx 2/T$ will not affect the high nonlinearity trend. In uniaxial extension

$$u_r = -0.5\dot{\epsilon}r, \quad u_\theta = 0, \quad u_z = \dot{\epsilon}z. \tag{4.32}$$

In this ideal flow, the velocity gradient $\nabla \boldsymbol{u}$ and $\dot{\boldsymbol{\gamma}}$ are

$$\nabla \boldsymbol{u} = \dot{\epsilon}\, diag\left(-\frac{1}{2}, -\frac{1}{2}, 1\right), \quad \dot{\boldsymbol{\gamma}} = \nabla \boldsymbol{u} + (\nabla \boldsymbol{u})^T = \dot{\epsilon}\, diag\,(-1, -1, 2). \tag{4.33}$$

The problem is reduced to solving the two components of the momentum balance in the r- and z-directions, noting that there is no spatial dependence under this idealised flow condition

$$\frac{\mathrm{d}\tau_{zz}}{\mathrm{d}t} = 2\dot{\epsilon}\tau_{zz} + \frac{2}{Ec}\dot{\epsilon} - \frac{\max(0,\ |\boldsymbol{\tau_d}| - Y_s)^{\frac{1}{n}}}{Ec}\frac{\tau_{zz}}{|\boldsymbol{\tau_d}|}, \tag{4.34}$$

$$\frac{\mathrm{d}\binom{\tau_{rr}}{\tau_{\theta\theta}}}{\mathrm{d}t} = -\dot{\epsilon}\binom{\tau_{rr}}{\tau_{\theta\theta}} - \frac{1}{Ec}\dot{\epsilon} - \frac{\max(0,\ |\boldsymbol{\tau_d}| - Y_s)^{\frac{1}{n}}}{Ec}\frac{\binom{\tau_{rr}}{\tau_{\theta\theta}}}{|\boldsymbol{\tau_d}|}. \tag{4.35}$$

The system of the three ordinary differential equations is solved numerically. The time evolution of τ_{zz} is shown on figure 3, for $n = 0.45$. The important finding from this simple analysis is that τ_{zz} scales like $(t_0 - t)^{n/n-1}$, irrespective of other parameters, like Ec, or Y_S in extreme nonlinearity, in other words it depends only on n.

The same figure demonstrates that elasticity through Ec affects only the prefactor of the asymptotic form, or, in other words, the intersection points of the asymptotic lines with the ordinate. Reducing Ec will require longer time to reach the region of high nonlinearity, where τ_{zz} scales as we calculated, but at the same point in time the axial stress is smaller.

Moreover, multiple tests were conducted by varying the exponent n with the same extension rate $\dot{\epsilon} = (2/T)$, and with $Ec = 0.1$ and $Y_s = 1$ to determine if the exponent in the scale $(t_0 - t)^{\alpha_3}$ will agree with our prediction of $(n/n - 1)$. Figure 4, clearly shows that this is the case for $n \in [0.3,\ 0.8]$.

5. Solution of the two-dimensional equations

We begin this section by validating the numerical algorithm we developed through a test case. Following this, we present the computed solution for the base material, including
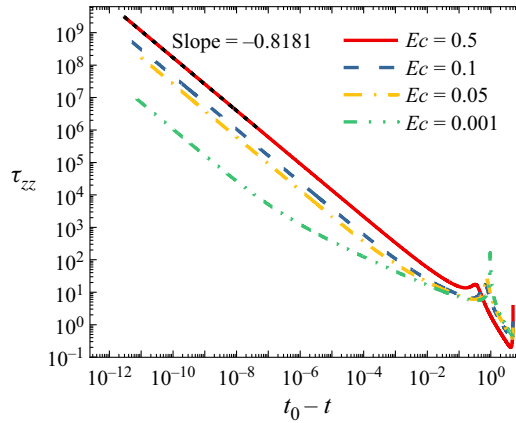
Figure 3. Evolution of the axial normal stress, τ_{zz}, vs. time to pinch in uniaxial extension flow with $\dot{\epsilon} = 2/t_0 - t$. The other EVP parameters are $n = 0.45$, $Y_S = 1$, resulting in $n/n - 1 = -0.8181$.
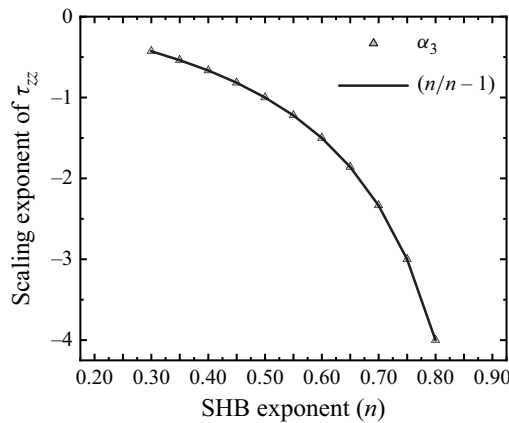

Figure 4. The scaling exponent of axial normal stress, τ_{zz}, vs. the SHB strain-rate-thinning exponent (n). The other EVP parameters are $Ec = 0.1$, $Y_S = 1$.

detailed examination of stress and velocity fields near the pinch point. We analyse the presence of universality and self-similar profiles. We conclude it by examining the impact of material parameters on the asymptotic behaviour.

5.1. *Accuracy of the numerical method*

To validate our numerical method, we compare our simulation results with those reported by Suryo & Basaran (2006) for a power-law material. In such a material, the viscosity is expressed as

$$\tilde{\mu}\left(\widetilde{\dot{\gamma}}\right) = \tilde{k}\left|\widetilde{\dot{\gamma}}\right|^{n-1},\tag{5.1}$$

where $\tilde{\mu}$ is the apparent power-law viscosity, $\tilde{k}$ is the consistency index and n is the power-law exponent. For flow without inertia, the aforementioned study predicts different flow regimes, depending on the value of n. Among them the most challenging one to capture is the so-called non-slender viscous power-law regime arising for $n < 0.54$, because the filament loses its slenderness and as n decreases, the strongly shear-thinning behaviour of the material leads to very fast pinch-off of the thread under capillary action. In this regime,
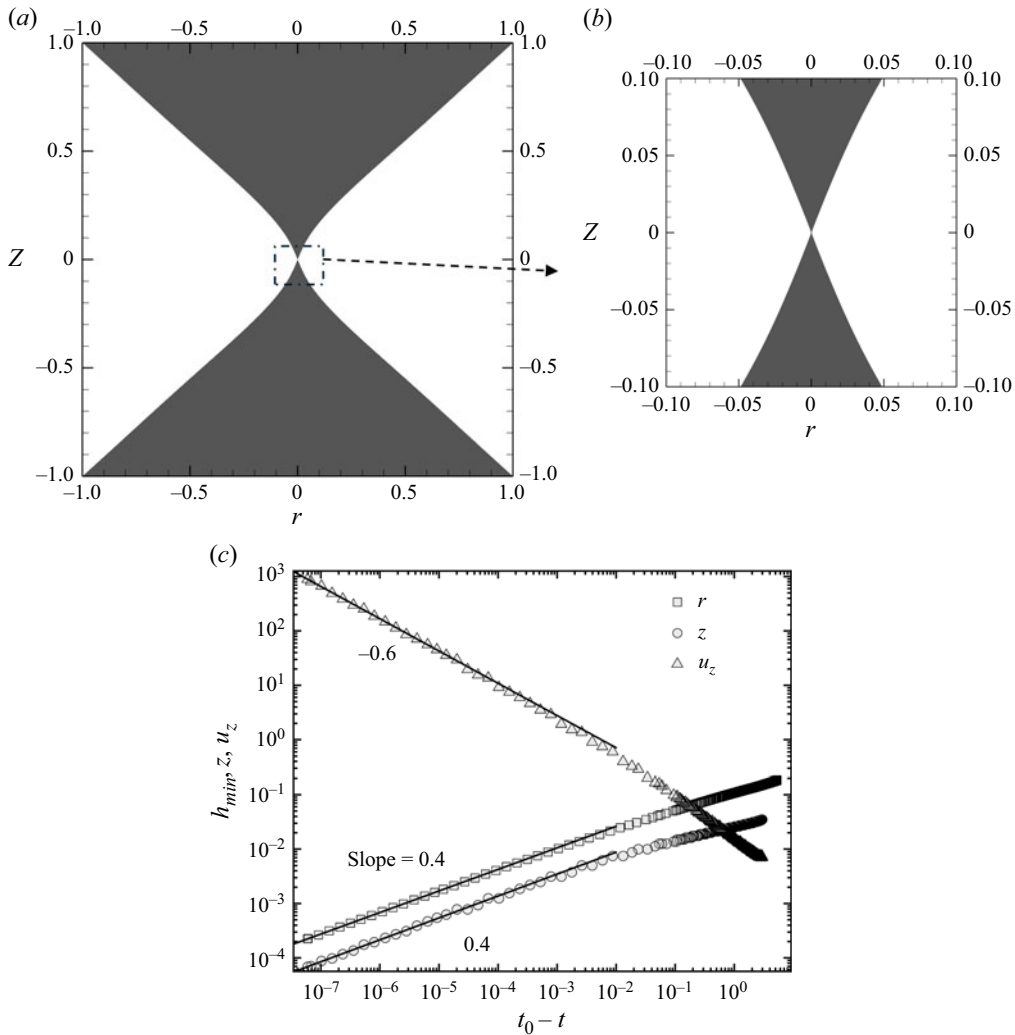
1020 A37-14

Figure 5. Pinching of a power-law thread with $n = 0.4$, $Oh^{-2} = 0$, $L = 2$, $U = 0$; (*a*) interface profile of the entire filament just before the breakup, (*b*) close-up near the pinch-off point, (*c*) minimum radius, axial position and velocity plotted as a function of time to pinch. The calculated slopes are in perfect agreement with the ones reported in Suryo & Basaran (2006).

the asymptotic scales are

$$h \sim T^n, \tag{5.2}$$

$$Z \sim T^n, \tag{5.3}$$

$$u_z \sim T^{n-1}. \tag{5.4}$$

We select $n = 0.4$, $Oh^{-2} = 0$, $L = 2$ to validate our numerical framework. The initial interface height is set as $h(z, 0) = 1 - 0.8 \cos(\pi z / 2)$. This perturbed interface suffices to initiate instability, even with a stationary upper disk ($u_{plate} = 0$), because of the absence of plasticity. Figure 5(*a*) shows the interface profile just before the breakup obtained with our numerical method and figure 5(*b*) illustrates a close-up view of the interface near the pinch point. Furthermore, figure 5(*c*) depicts the scaling of the minimum radius, axial velocity and axial position for the power-law thread. All scales in this figure are in perfect

1020 A37-15

Oh^{-2}	n	Y_s	Ec	U	L_0
0	0.45	1.25	0.14	0.39	2

Table 2. Parameters for the base case study.

agreement with those reported in Suryo & Basaran (2006). This demonstrates the validity and accuracy of our calculations.

5.2. *General time Evolution of an EVP filament*

We use the 0.2 % Carbopol solution produced and rheologically characterised by Lopez *et al.* (2017), as the material for our base case study. We used a nonlinear regression to determine the material parameters from their flow curve and frequency sweep test at 1 % strain amplitude, and we achieved close agreement with the rheological measurements. For a more detailed description, the reader is referred to Moschopoulos *et al.* (2021, 2023). The resulting parameter values for the base case study, are given in table 2, except for setting $Oh^{-2} = 0$, to simulate flow physics without inertia.

Figure 6 illustrates the time evolution of the EVP filament. Once the disks begin to move, the material yields in most of its length, as seen for example at $t = 1.32$. Near the disks though, the material only deforms elastically as a Kelvin–Voigt solid, because its initial velocity and stresses were set to zero everywhere and the no-slip and no-penetration conditions adhere the material to the disks, preventing the development of normal stresses as well. To identify the yielded regions, we employ the von Mises criterion, as detailed in § 2.1. Yielding occurs first at the plane of symmetry, where the stress magnitude is maximised and with the assistance of capillarity they form a neck there. At all times, the filament deformation retains the plane of symmetry at $z = 0$, because of the absence of gravity and inertia. As stretching continues, the neck gets thinner there making the velocity and stress gradients more pronounced. Simultaneously, rate thinning decreases the viscous resistance there, making the deformation larger and more local, $t = 2.75$. Consequently, deformation has to decrease away from the mid-plane, reducing the velocity and stress gradients. Where the stress magnitude drops below the yield condition again, the material will solidify, permitting deformation in a decreasing length of the bridge. This sequence of events can be seen in the first three panels of figure 6.

When h_{min} reaches approximately $O(10^{-2})$, the filament begins to deform even more rapidly, now driven primarily by capillarity. The faster escape of the material from the plane of symmetry through the increasingly smaller cross-section of the neck produces a jet-like, larger axial velocity away from the pinching region. With its increased axial velocity, this material now penetrates further inside the unyielded material away from the necking region, and toward the top moving solid disk, compressing it more effectively. In this area, the local increase in the radius is attributed to the continuous injection of material. This complex kinematics leads to material yielding away from the neck with a small unyielded area in between at time $t = 2.8978$. Before turning into the dynamics, we note the following: Because of axial symmetry, the radial velocity is zero at the axis of symmetry, but away from it and near the pinch point, at $z = 0$, it is negative following the decrease in radius, whereas in the corner region (close to highest curvature of the interface), it becomes positive. Consequently, close to the pinch point, τ_{rr} is negative but it turns positive in the vicinity of the corner region, explaining the sign change of τ_{rr} in this area; see figure 7 below. The same reasoning applies to the change of the sign of τ_{zz} and τ_{rz}. The sign change of all stresses indicates that, close to the corner region, the
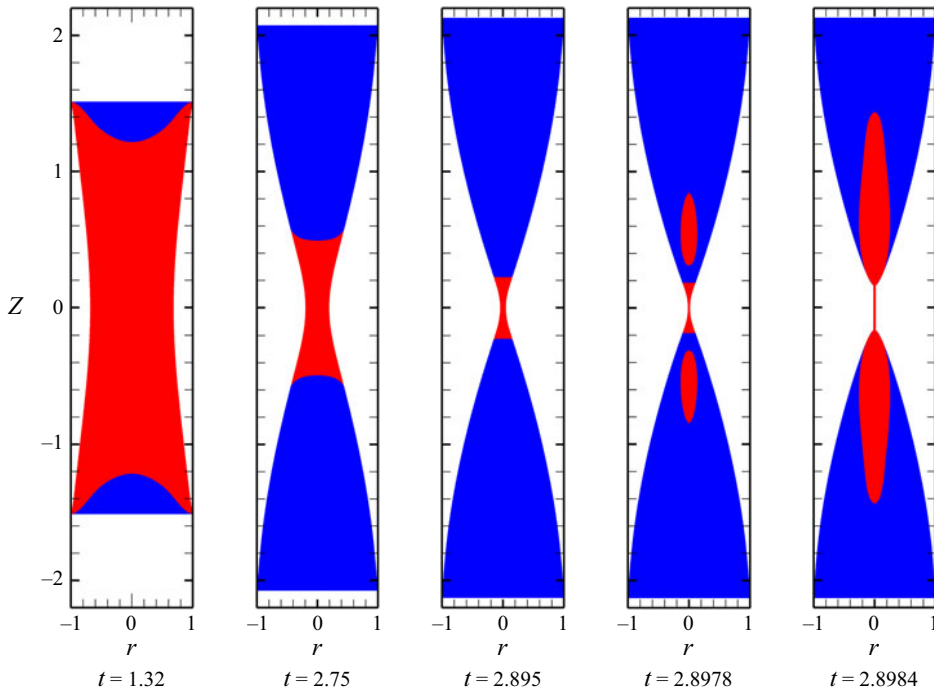
Figure 6. Time evolution of filament under constant stretching with $U = 0.39$. The red and blue areas indicate yielded and unyielded regions, respectively. The other parameters are $Oh^{-2} = 0$, $n = 0.45$, $Y_s = 1.25$, $Ec = 0.14$, $L_0 = 2$.

components of the deviatoric stress tensor will approach zero. Hence, the transition region contains unyielded material that separates the yielded neck from the yielded island further up. As the filament approaches breakup, velocity and stress magnitude increase even faster and the unyielded area in the transition region shrinks in size and eventually disappears, as shown in figure 6, at $t = 2.8984$. It is worth mentioning that this is observable in EVP materials, because they can deform even in unyielded regions.

Figures 7(*a*) and 8(*a*) present contours of velocity and extra stress tensor components, along with the second invariant of the extra stress tensor, just before pinch-off at $t = 2.8984$. These plots clearly illustrate that extremely high velocity and stress magnitudes arise in the necking region. Moving away from this region, all values rapidly decrease until they match the boundary conditions imposed on the solid plate. Figures 7(*b*) and 7(*c*) depict contours of velocity components focusing at the corner and necking regions of the interface, respectively. In the necking region, the axial velocity u_z dominates, becoming three orders of magnitude larger than the radial velocity u_r. This dominance decreases when approaching the corner region, with its magnitude being only one order of magnitude higher than that of u_r.

As demonstrated in figures 7(*c*) and 7(*d*), the magnitudes of τ_{rr} and $\tau_{\theta\theta}$ are nearly identical in both magnified regions, with their extrema occurring at the necking region. This is consistent with the fact that (du_r/dr) and (u_r/r) also attain their maximum value in this region. The pressure magnitude in the necking region is proportional to $(1/h)$, implying that the high pressure within this region decreases progressively as the distance from the symmetry plane increases. This trend is clearly illustrated in figures 8(*b*) and 8(*c*), which show pressure contours in the magnified corner and necking regions, respectively. The shear stress component τ_{rz} reaches its extremum in the corner region, approximately
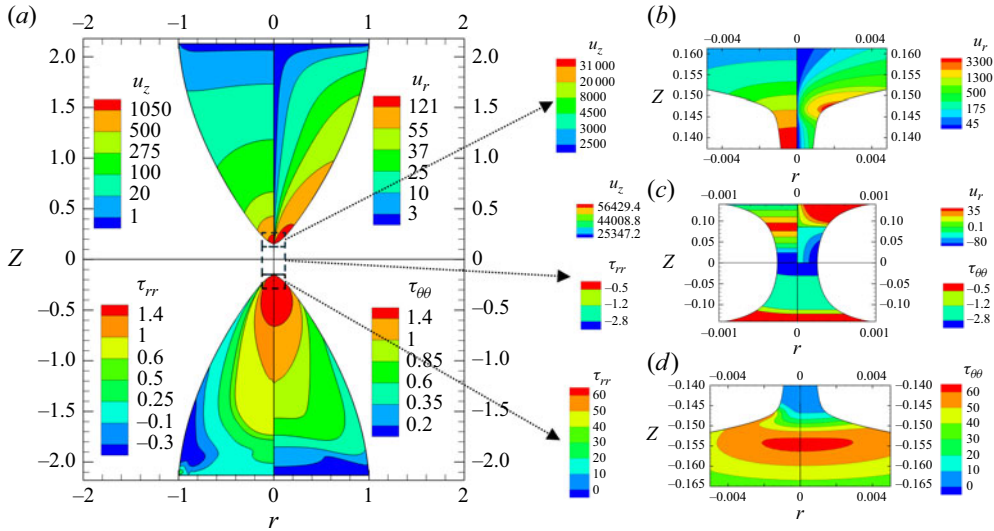
Figure 7. Contours of velocity and stress components of the filament under constant stretching with $U = 0.39$ just before pinch-off, at $t = 2.8984$. Other parameters are $Oh^{-2} = 0$, $n = 0.45$, $Y_s = 1.25$, $Ec = 0.14$, $L_0 = 2$.
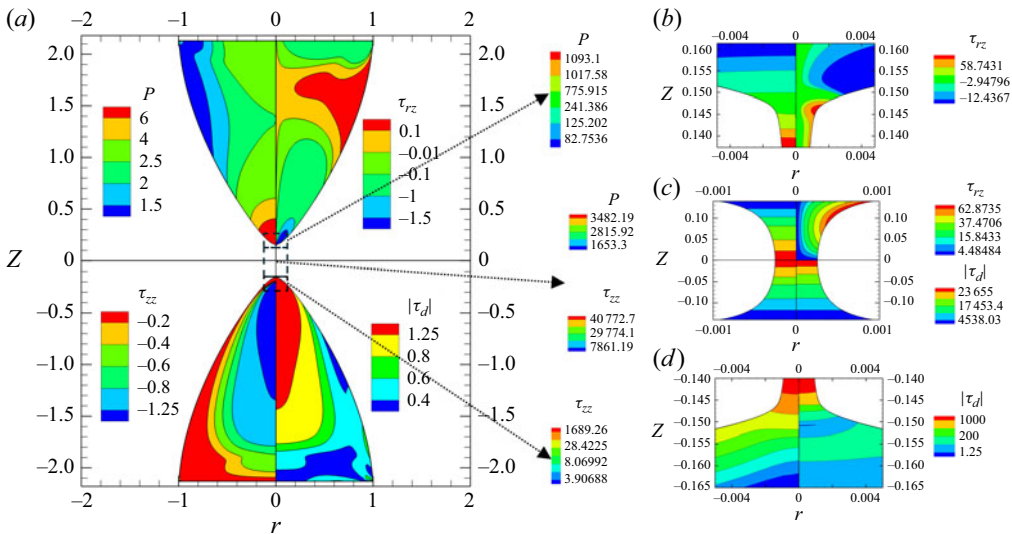

Figure 8. Contours of pressure and stress components of the filament under constant stretching with $U = 0.39$ just before pinch-off, at $t = 2.8984$. Other parameters are $Oh^{-2} = 0$, $n = 0.45$, $Y_s = 1.25$, $Ec = 0.14$, $L_0 = 2$.

at the point of highest interface curvature. Figure 8(b) further reveals that τ_{rz} exhibits a magnitude comparable or even slightly higher than τ_{rr} and $\tau_{\theta\theta}$ in this region. The extension-dominated nature of filament breakup is evident in the contours of τ_{zz} in necking and corner regions, as shown in figure 8(c) and 8(d). Similar to the axial velocity, τ_{zz} is three orders of magnitude higher than all other stress components in the necking region but rapidly decreases until it becomes comparable to τ_{rz} at the corner. The magnitude of the second invariant of the extra stress tensor in the thread is approximately $(1/\sqrt{3})|\tau_{zz}|$, see figure 8(c); However, this relation no longer holds beyond the neck region, as depicted

in figure 8(*d*). The variation in the radial direction inside the neck for all variables is negligible. One may observe a small radial variation of u_r, τ_{rz} and τ_{rr}, but only because their magnitude is much smaller than that of the other variables and the range of colours in each panel depends on the range of variation of the corresponding variable. In the supplementary material SM2, we present the time evolution of the axial stress component τ_{zz} and the axial velocity u_z, where one can easily observe that they increase from $O(1)$ to $O(10^5)$ without any oscillations in their contours, during the same simulation.

All these justify the assumptions made to derive the slender filament equations in the necking region. However, we will not employ the slender filament equations for simulating this flow. As stated by Moschopoulos *et al.* (2020), in stretching of viscoplastic filament, the deviation between 2-D and slender filament simulations increases as the viscoplastic character of the flow becomes more pronounced. We believe this applies for EVP material as well and verifying the accuracy of the solution obtained by the slender equations requires extensive analysis, particularly for different combinations of Y_s and Ec. Moreover, aside from the necking region, the filament is not slender throughout, particularly in the corner region, necessitating a full 2-D analysis for accurate results. Additionally, the slender filament approximation, neglects τ_{rz}, which is inappropriate given that τ_{rz} is of the same order of magnitude or larger than τ_{rr} and $\tau_{\theta\theta}$ in this region; see also Eggers, Herrada & Snoeijer (2020).

5.3. *Determination of pinch-off time, t_0*

Accurate approximation of the pinch-off time, t_0, is most important, because even a very small error in determining its value will lead to incorrect calculation of the asymptotes. Moreover, in our arbitrary Lagrangian Eulerian formulation, breakup cannot occur without external intervention, which must take place as close as numerically possible and physically allowed to the pinch-off time. Computational experiments as well as other studies suggest that, in order to accurately determine it, simulations have to be conducted until the minimum radius becomes approximately five orders of magnitude smaller than the initial radius, or, in the present dimensionless form, when $h_{min} = 10^{-5}$. Then the very last time instant of the simulation can be considered as pinch-off time and the scalings are correctly determined. On the other hand, when the minimum radius reaches approximately $O(10^{-3})$, the EVP stresses grow very fast because of the viscoelastic nature of the EVP material, making the resulting system of equations extremely stiff to solve. Although reaching values as small as $h_{min} = 10^{-5}$ may not be feasible, we have employed a least-squares, nonlinear regression method to extrapolate the pinch-off time.

The extrapolation to the breakup time is based on the asymptotic form obtained in § 4.1 for $h_{min} = \phi_0(t_0 - t)^{\alpha_1}$. Treating ϕ_0, t_0 and α_1 as fitting parameters, we apply this power-law function to the minimum radius data over the last 100 computed time steps. Figure 9 depicts the regression applied to the minimum radius as a function of time for the base case study. The computed t_0 for this case is found to be 2.8984063, while $\Phi_o \approx 10.7$ and $\alpha_1 = 0.8$

The calculated t_0 is then used to generate plots of h_{min}, z, u_z, τ_{zz} versus T. According to § 4.1, the axial stress τ_{zz} should scale as $(t_0 - t)^{(n/n-1)}$. Owing to conservation of momentum and the balance between capillarity and axial stresses, the minimum radius should decrease asymptotically as $(1/\tau_{zz})$, in other words as $h_{min} \sim (t_0 - t)^{(n/1-n)}$. Furthermore, to satisfy the slender jet continuity equation, the axial position and velocity must scale like $(t_p - t)^{\delta}$ and $(t_p - t)^{1-\delta}$, respectively. Figure 10 illustrates in log–log scales h_{min}, z, u_z, and τ_{zz} versus $t_0 - t$ for $n = 0.45$, $Ec = 0.14$, $Y_s = 1.25$, $U = 0.39$. The linear slope in figure 10 verifies that, indeed, a power-law relation exists for all variables. The
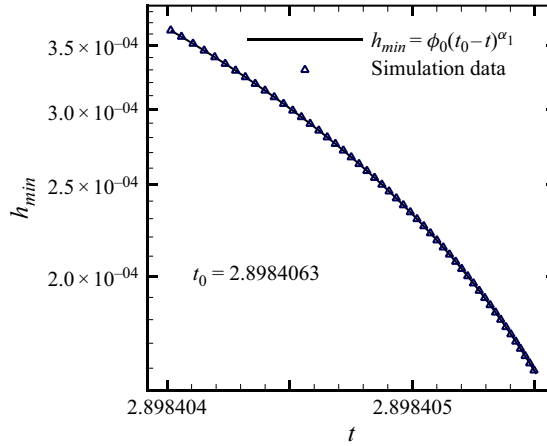
Figure 9. Nonlinear regression employed to extract the pinch-off time, t_0, from the numerical results of the base case study, for $Oh^{-2} = 0$, $n = 0.45$, $Y_s = 1.25$, $Ec = 0.14$, $L_0 = 2$.
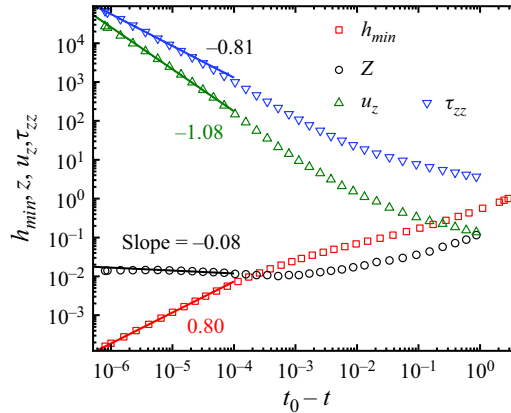

Figure 10. Decay of the minimum radius, growth of axial velocity, axial position and axial stresses as pinching time is approached for $Oh^{-2} = 0$, $n = 0.45$, $Ec = 0.14$, $Y_s = 1.25$, $U = 0.39$ $((n/1 - n) = 0.818)$. The slopes determine the corresponding exponents of the power-law scaling functions.

calculated slopes are h_{min}, Z, u_z and τ_{zz} are 0.80 ($\approx (n/1 - n)$), -0.08 ($= \delta$), -1.08 ($= \delta - 1$) and -0.81 ($\approx n/n - 1$), respectively. These slopes represent the exponents of power-law scaling functions for the base material and they are in perfect agreement with the asymptotes we derived with the elasto-capillary scalings, as discussed earlier.

5.4. *Self-similar forms of the two-dimensional solutions*

Given a distinct set of parameters (n, Ec, Y_s), first we calculate the scaling exponents for minimum radius, axial position, axial velocity and stress, as shown in figure 10, then we rescale these variables accordingly at different times to verify their collapse onto a single curve, completing in this way the demonstration of the existence of self-similarity. We have observed that this holds for a range of power-law exponents, but, for conciseness, next we present only a single set of parameters corresponding to the base case study. The inset to figure 11 shows interface profiles for five different values of minimum radius h_{min}. Figure 11 depicts that these transient interface profiles obtained by 2-D simulations
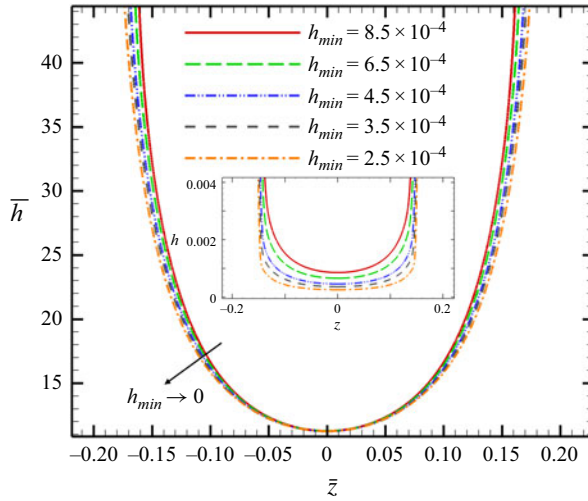
1020 A37-20

Figure 11. (Inset) Transient interface shape obtained by 2-D simulations at five different h_{min} values. (Main figure) Rescaled interface using the numerically determined scaling laws for the same five h_{min} values. The main figure illustrates convergence to a self-similar interface profile. The very large difference in the magnitudes of h before and after scaling is noteworthy.
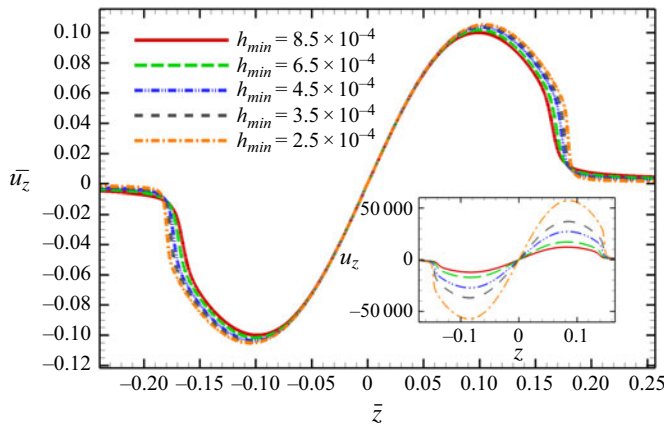

Figure 12. (Inset) Transient velocity variation along axial coordinate (z) at the interface obtained by 2-D simulations at five different h_{min} values. (Main figure) Rescaled velocity plotted against rescaled axial coordinate using the numerically determined scaling laws for the same five h_{min} values. The main figure demonstrates convergence to a self-similar velocity profile. The very large difference in the magnitudes of the velocity before and after scaling is noteworthy.

collapsing onto a single self-similar interface profile by rescaling the interface height $\overline{h} = (h/(t_0 - t)^{(n/1-n)})$ and the axial position $\overline{Z} = (z - z_0/(t_0 - t)^{\delta})$, where $\delta \approx -0.08$. Please note that the rescaled variables are denoted by an overbar () over the corresponding variable symbol.

The inset to figure 12 shows the variation of axial velocity u_z at the interface versus the axial coordinate z for five different values of minimum radius h_{min}. Figure 12 depicts that by rescaling the axial velocity as $\overline{u}_z = (u_z/(t_0 - t)^{\alpha_2})$, with $\alpha_2 = -1.08$, the transient velocity profiles collapse onto a single self-similar profile as the minimum radius $h_{min} \to 0$.
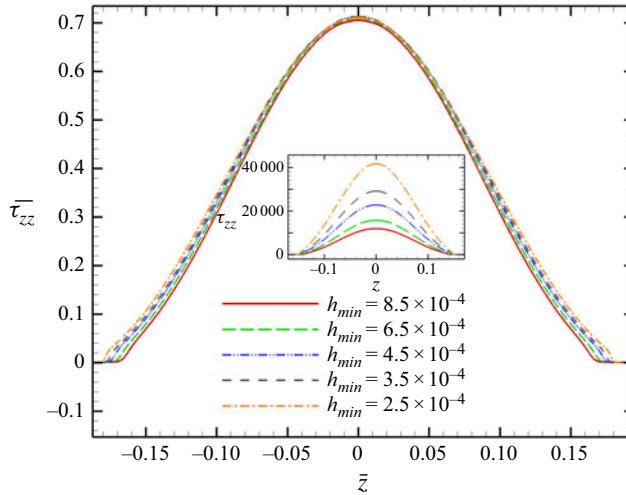
Figure 13. (Inset) Transient axial stress variation along axial coordinate (z) at the interface obtained by 2-D simulations at five different h_{min} values. (Main figure) Rescaled axial stress plotted against rescaled axial coordinate using the numerically determined scaling laws for the same five h_{min} values. The main figure demonstrates convergence to a self-similar axial stress profile. The very large difference in the magnitudes of stress before and after scaling is noteworthy.

Finally, the inset to figure 13 shows the axial stress τ_{zz} versus the axial coordinate extracted from nodal values of 2-D calculations at the interface for five different values of h_{min}. The rescaled axial stress $\overline{\tau}_{zz} = (\tau_{zz}/(t_0 - t)^{(n/n-1)})$ vs. rescaled axial coordinate does converge to a self-similar profile, as shown on figure 13.

The plots in this section show good collapse near $\overline{Z} = 0$; however, the quality of the collapse diminishes as $\overline{Z}$ increases. This can be attributed to the negative value of the exponent δ, which leads to smaller values of $\overline{Z}$ compared with cases where $\delta > 0$. As illustrated in the scaling plot of figure 10, the axial position increases as breakup is approached. Consequently, in self-similarity plots, the span of $\overline{Z}$ is reduced relative to other constitutive equations, such as Newtonian or power-law fluids, for which $\delta > 0$.

Moreover, we have extracted numerically scaling laws for the variables in the corner region. However, they do not follow a universal scaling law, we were unable to derive analytically these scalings nor could we obtain self-similar solutions. It is possible that this is caused by the fact that the corner region involves in the thread side yielded material until the very late stages of breakup, much later than when asymptotic behaviour of the neck starts, but unyielded material in the other side toward the disc. Consequently, derivation of the asymptotics is not straightforward, because the material exhibits dual behaviour in this region. Additionally, since the solvent viscosity is set to zero in this study, the dominant balance and self-similar form of the governing equations become more complex than those reported by Fontelos & Li (2004) for the Giesekus fluid.

5.5. *Parametric analysis*

We will separate this section based on the value of the power-law index. When $0.43 < n < 1$, surface tension is the main driving force causing breakup. This range of values is examined in §5.5.1. Although for $n > 0.5$, the SHB model predicts extension rate hardening, which is not expected for Carbopol (Kordalis *et al.* 2021), we will examine values of n up to one for a more complete study. Values of $0.33 < n < 0.43$ will be examined separately in §5.5.2, because then capillarity plays no role in pinching-off,
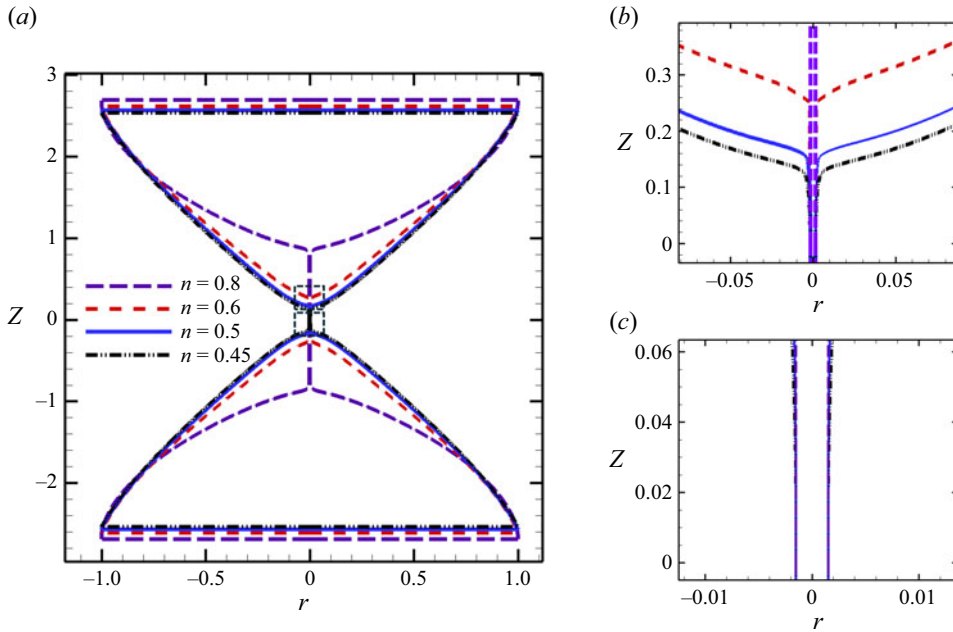
Figure 14. Profiles of the entire filament (*a*) and closeup views in the corner (*b*) and necking (*c*) regions for four different values of *n*. In (*b*) we did not include the entire 'local' interface for $n = 0.8$, because it would reduce the clarity of the rest. The remaining parameter values are $Y_s = 0.1$, $Ec = 0.14$, $U = 0.1$.

while $n = 1$ will be examined in § 5.5.3, also separately, because, as we will demonstrate, pinching-off does not take place in the Saramito–Bingham model (Saramito 2007). We will examine the effect of *n* and *Ec*, where appropriate. Here, Y_s has no effect, because the thread during pinching-off is yielded throughout.

5.5.1. *Elasto-plasto-capillary breakup regime,* $0.43 < n < 1$

Although the YS does not enter the dominant balance determining the asymptotic behaviour of the thread in this regime, the title includes the term 'plasto', because part of the included elastic term is what remains from the viscoplastic contribution in the constitutive law, see (3.11).

5.5.1.1. Effect of strain-rate-thinning exponent (n). We proceed by examining the effect of the strain-rate-thinning exponent, *n*, on the pinch-off dynamics. Figure 14(*a*) depicts interface profiles for four different values of *n*, recorded when $h_{min} = 1.5 \times 10^{-3}$.

As *n* increases, strain-rate thinning decreases, resulting in increasing elastic stresses, including its radial normal component, which opposes capillarity. This leads to a longer thread around the middle of the filament for the same h_{min}, as depicted more clearly in figure 14(*b*). Given that the initial dimensions of the filament for all cases are the same, a longer neck causes a slight increase in the total height of the filament (see figure 14*a*), when it has reached the same h_{min} under the same constant stretching velocity. Additionally, the increased opposing elastic force slows down the breakup rate, causing the EVP thread to break later in time as *n* increases. Figure 14(*c*) shows that the interface profile close to pinch off is almost a perfect cylinder for all values of *n*.

The dependence on time to pinch of the minimum radius, the axial normal stress and axial velocity, as well as the length of the neck up to which its radius increases by only 1 % from its minimum value, are presented in figure 15. Figures 15(*a*) and 15(*b*) depict
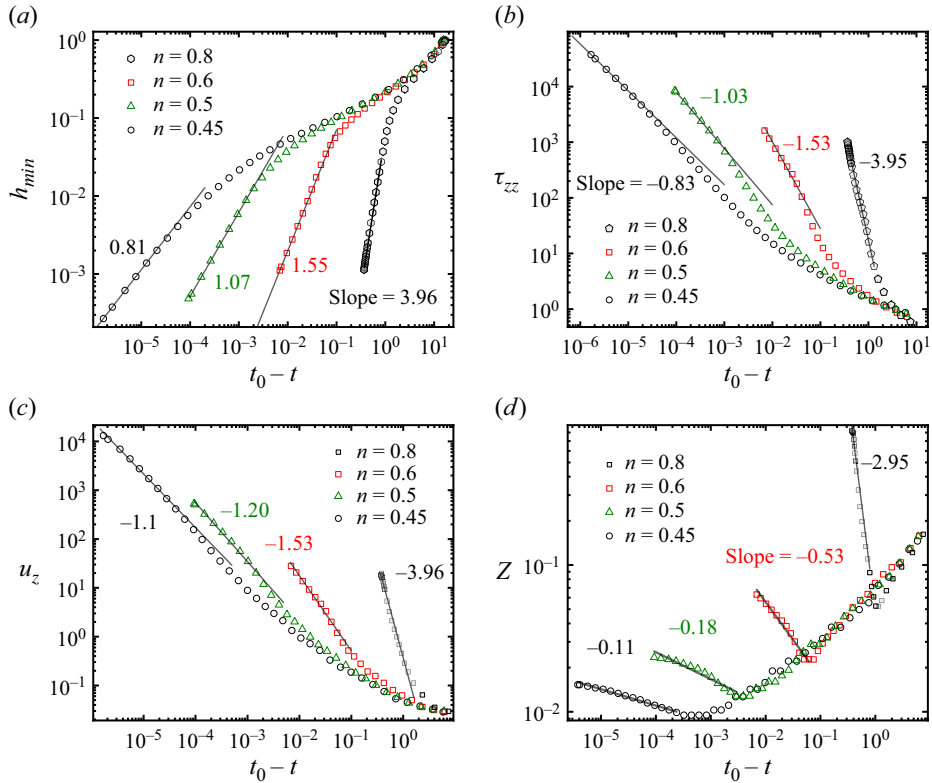
Figure 15. Effect of the exponent of strain-rate thinning on the scaling with respect to $(t_o - t)$ of minimum radius (a), axial stress (b), axial velocity (c) and axial length of neck (d). The rest of the parameter values are $Y_s = 0.1$, $Ec = 0.14$, $U = 0.1$.

the h_{min} decrease and the τ_{zz} increase as a function of time to pinch $t_o - t$. Focusing on their values when they reach their asymptotic behaviour, one readily observes that they follow very closely the power-law dependence on n, namely $\pm n/(1 - n)$ for all four values of n. The calculated slopes, which represent the exponents of the power-law scaling functions, are almost in perfect agreement with the proposed asymptotes. An error of $\pm 2\%$ from the earlier predicted asymptotes may be attributed to inaccuracies of the numerical method and a slight radial dependence of the variables in the numerical solution of the 2-D equations. As these exponents require, when n increases, the slopes of the asymptotes of both variables increase. Figure 15(a) also shows that increasing n brings h_{min} faster to a certain small value, although the time to breakup is delayed, since this occurs at larger values of $(t_o - t)$. Similarly, figure 15(c), demonstrates that the slope of the asymptotic increase of v_z increases with n, although for $n < 0.5$, the exponent does not have an analytic relation with it; see (3.27) and (3.28). Finally, figure 15(d) indicates that the thread of the filament becomes longer at a faster rate, when n increases. This length extends from the plane of symmetry to the axial position where $h = 1.01h_{min}$, and it is denoted as Z.

Altogether, figure 15 demonstrates that, for smaller n values, the asymptotic behaviour is reached when calculations are carried out to times much closer to breakup. This leads to a thinner neck, driven by higher velocity produced by higher axial stress. Another important observation from these four panels is the sharp increase in the extreme values reached by h_{min}, v_z and τ_{zz} as n decreases. These values are $\sim 2 \times 10^{-4}$, 2×10^4 and 5×10^4,
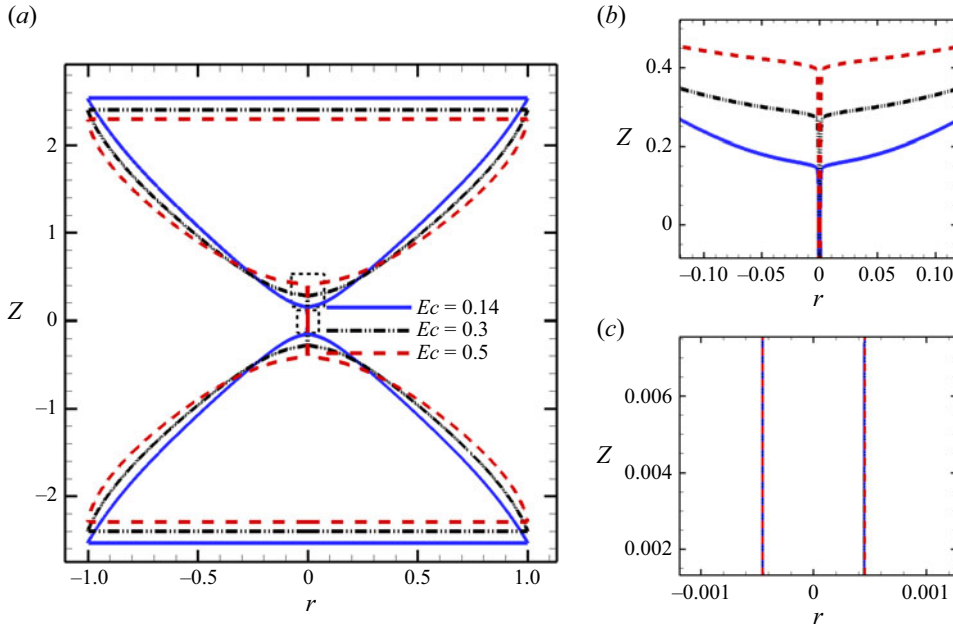
Figure 16. Profiles of the entire filament (*a*) and closeup views in the corn (*b*) and necking (*c*) regions for three different values of Ec. The rest of the parameter values are $Y_s = 0.1$, $n = 0.45$, $U = 0.1$.

respectively, for $n = 0.45$, while their initial values are 1, 0 and 0, respectively. This makes plain how challenging these calculations are and the importance of the new ideas adopted in the particular numerical algorithm.

5.5.1.2. Effect of elastic modulus. We move on by examining the effect of the elasto-capillary number, Ec, on the pinch-off dynamics. Figure 16 illustrates the different shapes of the filament when $h_{min} = 4.5 \times 10^{-4}$.

Focusing on figure 16(*a*), we observe that increasing Ec generates both a shorter filament and, hence, one that breaks faster, but a longer thread around the plane of symmetry. This seemingly contradictory trend is explained as follows: increasing Ec affects both the unyielded and yielded regimes of the filament in different ways. To start with, when Ec increases, the filament deforms more as an elastic solid prior to yielding, allowing for a more localised viscoelastic deformation in the region around the plane of symmetry. This leads to earlier formation of the neck and earlier breakup of the filament, although the opposing elastic forces also increase. All these lead to a shorter total filament height at pinch-off time, figure 16(*a*). This increased elastic yielding has been reported also by Moschopoulos *et al.* (2023), where the bulk dynamics has been studied. The same increase in Ec increases τ_{zz}, which accelerates the evacuation of the neck and the decrease of its radius. At the same time, the larger normal stresses generate a longer neck, because they oppose neck thinning by capillarity, as shown on closeup view at the corner region, figure 16(*b*). Figure 16(*c*) shows that the neck profile close to pinch off forms a nearly perfect cylinder for all values of Ec.

The trends in h_{min} decay and τ_{zz}, v_z, and Z growth are presented in figure 17. The slopes of all four variables with respect to the time to pinch ($t_o - t$) in the asymptotic regime depend only on n, but are independent from Ec. The elastocapillary number affects only the intersection with the ordinate, via affecting the coefficient ϕ_0 in (3.20). Even this effect is weak for all variables, except for Z. Indeed, figure 17(*d*) indicates that the axial extent
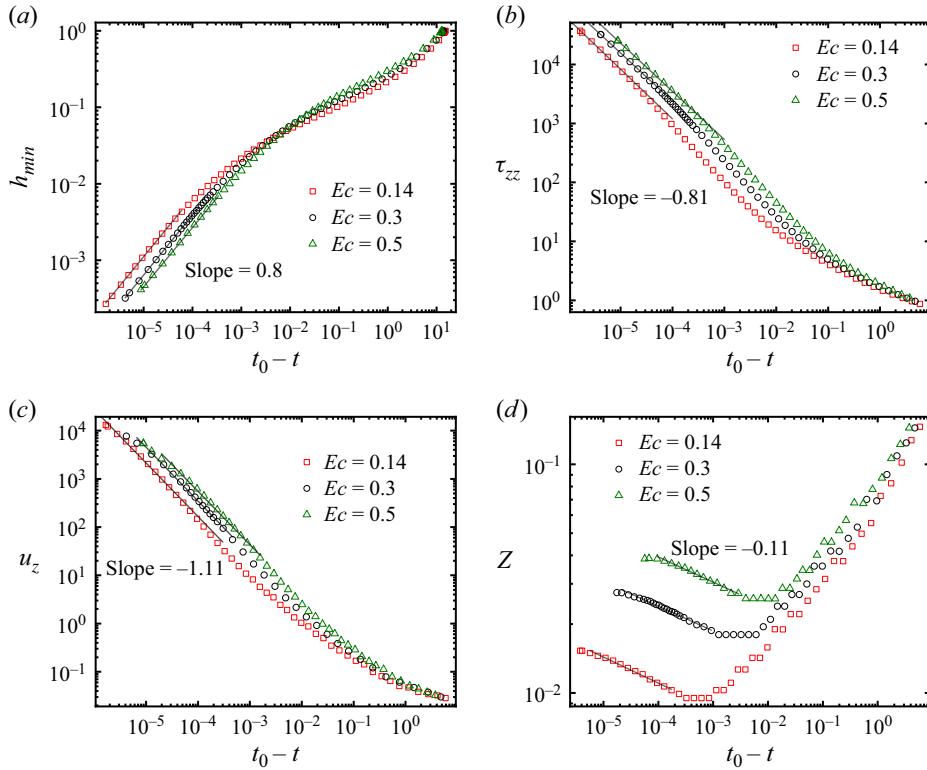
Figure 17. Effect of Ec on the scaling with respect to $(t_o - t)$ of minimum radius (*a*), axial stress (*b*), axial velocity(*c*) and axial length of neck (*d*). The rest of the parameter values are $Y_s = 0.1$, $n = 0.45$, $U = 0.1$.

over which this scaling holds is longer, or, in other words, the neck is longer for higher Ec, although its growth rate remains the same. The calculated slopes, which represent exponents of the power-law scaling functions, are almost in perfect agreement with the proposed asymptotes.

5.5.2. *Elasto-plastic breakup regime,* $0.33 < n < 0.43$

In this section we will examine the pinching dynamics of materials with smaller power-law exponent $0.33 < n < 0.43$ and with as low n values (always positive) as our algorithm allows with convergence in a reasonable time. As in the previous regime, the YS does not enter the dominant balance in this regime either, but its title again includes the term 'plastic', because part of the appearing elastic term is what remains from the viscoplastic term in the constitutive law. A small decrease in n below 0.45 leads to a significant deviation from the asymptotic result for the minimum radius. For the values of $0.33 < n < 0.43$, the breakup mechanism is no longer governed by capillarity. Instead, it is dictated purely by elastic stresses, which drive the breakup after the neck is formed. This type of pinching-off has been identified by Renardy ([2002a](#)) for the generalised form of PTT materials that he introduced. To further investigate this regime, we carried out filament stretching simulations for three different values of n where $0.33 < n < 0.43$. In the elasto-plastic breakup regime, the minimum radius follows a different asymptotic scaling
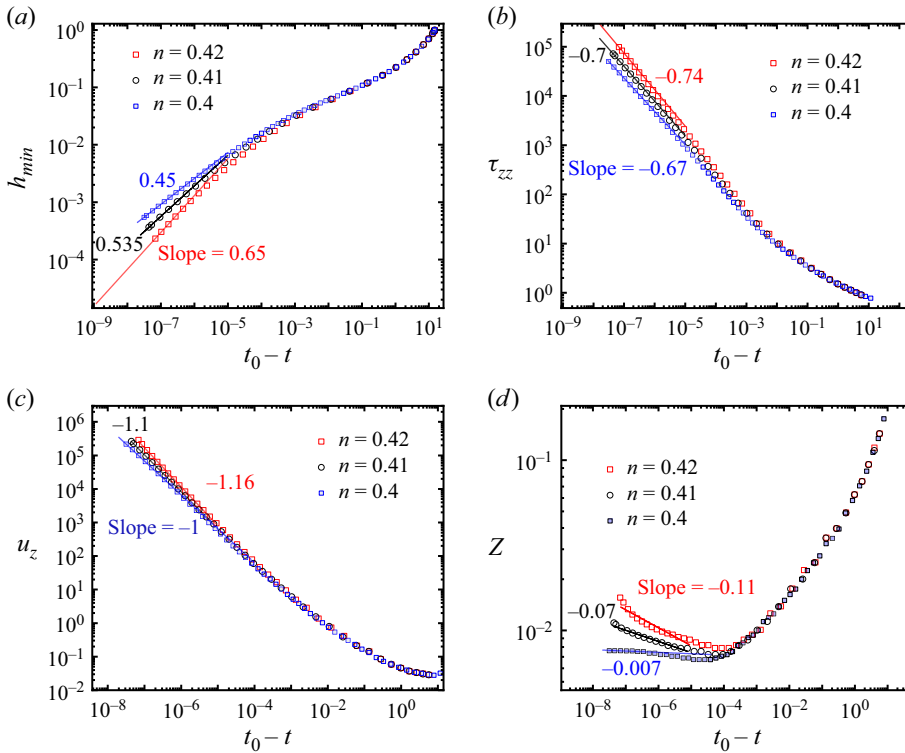
Figure 18. Effect of the exponent of the strain-rate thinning (n) in elastic breakup regime on the scaling with respect to $t_0 - t$ of minimum radius (a), axial stress (b), axial velocity (c) and axial length of neck (d). The rest of the parameter values are $Y_s = 0.1$, $Ec = 0.14$, $U = 0.1$.

$h_{min} \sim (t_0 - t)^{(n/4-8n)}$. However, since surface tension does not appear in the constitutive equation, the scaling for τ_{zz} remains unchanged, following $\tau_{zz} \sim (t_0 - t)^{(n/n-1)}$.

This is shown in figures 18(a) and 18(b), respectively. Additionally, our calculations indicate that, by decreasing the value of n, the axial velocity and axial position scaling exponents, α_2 and δ approach the values of -1 and 0, respectively, as illustrated in figures 18(c) and 18(d), respectively. The exponents in this regime do not depend on Ec, similar to the capillary-driven regime, and the corresponding results are omitted for conciseness. It is noteworthy that reaching the asymptotic range now requires getting even closer to the breakup time $(t_0 - t) < 10^{-5}$ and fully capturing it requires approaching small T values more than ever before, down to $(t_0 - t) \sim 10^{-8}$. All these necessitate extremely small time steps for accurate predictions. Furthermore, the extreme values of h_{min}, v_z and τ_{zz} now become $\sim 3 \times 10^{-4}$, 5×10^5 and 2×10^5, respectively, with the last two approximately one order of magnitude larger than their values for $n = 0.45$. All these observations reveal that the calculations become increasingly difficult as n decreases. The deviation in the scaling exponent α_1 for $n = 0.4$ is most pronounced among all cases studied. Specifically, our numerical results yield $\alpha_1 = 0.45$, whereas the asymptotic scale predicted from slender filament equations is 0.5. Even with a more refined mesh in the necking region, including more than 10 000 axial elements results in the same value of $\alpha_1 = 0.45$. We believe this deviation arises by the factors discussed earlier.

n	α_1	δ	$\alpha_1 - \delta$
0.4	0.45	−0.0	0.45
0.45	0.81	−0.11	0.92
0.5	1.07	−0.18	1.25
0.6	1.55	−0.53	2.08
0.8	3.96	−2.95	6.91

Table 3. Values of exponents α_1, δ and $\alpha - \delta$ for five different SHB exponents. The rest of parameters are $Y_s = 0.1$, $Ec = 0.14$, $U = 0.1$.
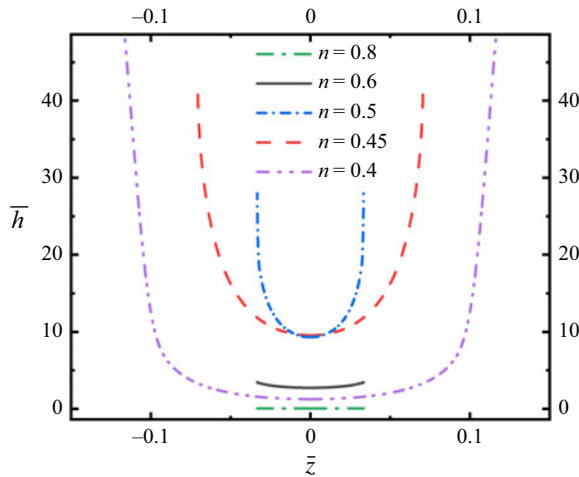

Figure 19. Self-similar interface profiles of EVP fluids with five different strain-rate-thinning exponents. The rest of the parameters are $Y_s = 0.1$, $Ec = 0.14$, $U = 0.1$.

5.5.3. *Collapse of filament shapes and radial velocity asymptotes for all cases with, $n < 1$*

Having analysed the scalings where the SHB exponent, n, is less than unity, we now present self-similar interface profiles obtained by 2-D simulations for various values of n, shown in figure 19. We have shown that z scales as $(t_0 - t)^\delta$ and that when n increases, δ increases in absolute value, remaining negative. Consequently, the rescaled axial coordinate $\overline{Z}$ spans a narrower region as n increases. Similarly, the span of $\overline{h}$ decreases. Both are clearly seen in figure 19. The local slenderness of the necking region decreases progressively with decreasing n. This trend can be understood by examining the ratio of radial to axial length scale, given by $(h_{min}/z) \sim (t_0 - t)^{\alpha_1 - \delta}$. The variation of the exponent $\alpha_1 - \delta$ is provided in table 3, revealing a sharp decrease from ~ 7 to 0.45 as n decreases from 0.8 to 0.4. Consequently, the breakup dynamics in the necking region exhibits an abrupt transition from a fully acceptable slender filament one to one that increasingly approaches a non-slender breakup at $n = 0.4$.

Figure 20 shows the evolution of the radial velocity at the interface on the symmetry plane as a function of remaining time to pinch, $t_0 - t$. Results from 2-D simulations reveal that, for all values of the SHB exponent (n) less than unity, the scale of u_r is $\alpha_1 - 1$. So, the radial velocity exhibits an asymptotic scale $u_r \sim (h_{min}/(t_0 - t))$, being valid for all cases where $n < 1$. Interestingly, as shown in figure 20, for SHB exponents $n > 0.5$, the absolute radial velocity $|u_r|$ at the interface on the symmetry plane decreases considerably as $t_0 - t \to 0$, indicating an increase in material's resistance to breakup,
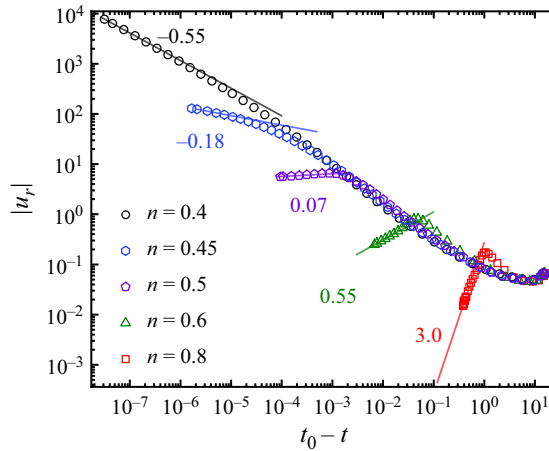
Figure 20. Variation of the radial velocity magnitude at the intersection between the symmetry plane and the interface with $t_0 - t$. The rest of the parameters are $Y_s = 0.1$, $Ec = 0.14$, $U = 0.1$.

which is a characteristic of extension-rate-thickening behaviour. Conversely, for $n < 0.5$, $|u_r|$ increases toward breakup, reflecting a significant reduction in elastic resistance, corresponding to extension-rate-thinning behaviour.

5.5.4. *Discrimination between finite-length and point breakup*

In this section we elaborate further on the discussion in § 4.1 concerning the finite-length breakup. We investigate this phenomenon by examining the filament thickness h at two axial locations; one at the plane of symmetry, where h attains its minimum value, and another one slightly above it at $z^+ = 0.01$. Initially, we attempted to demonstrate finite-length breakup by plotting h_{z+} and h_{min} as functions of time t or time to breakup $t_0 - t$. However, the near perfect overlap of these curves hindered any definitive conclusion. Next, we employed an alternative metric by plotting the normalised difference of filament thickness probed at these two axial locations versus time to breakup

$$\chi_h = \frac{h_{z+} - h_{min}}{h_{min}}. \tag{5.5}$$

This quantity may also be experimentally accessible. If a line is drawn connecting these two points on the interface, one at $z = 0$ and the other at $z = z^+ = 0.01$, the difference $h_{z+} - h_{min}$ is proportional to the absolute slope of that line, since Δz is fixed. A decrease in $h_{z+} - h_{min}$ indicates that the filament shape is becoming more cylindrical. Meanwhile, the decay rate of h_{min} characterises the rate at which breakup occurs at the symmetry plane. Therefore, an increase in χ_h as $t_0 - t \rightarrow 0$ denotes that the rate of filament thinning leading to point breakup exceeds the rate at which a cylindrical 'inner thread', if present, is formed. In this context, a negative slope of χ_h plotted against $t_0 - t \rightarrow 0$ in log–log plot implies that breakup will asymptotically precede the formation of a cylindrical neck, if such neck is formed at all. Conversely, a positive or zero slope suggests finite-length breakup, wherein the filament retains a finite axial extent close to breakup. Asymptotically, this implies that the cylindrical neck forms either before breakup, if $\chi_h \rightarrow 0$, or simultaneously with it, if χ_h approaches a constant. As shown in figure 21, χ_h increases near breakup for both a power-law material with $n = 0.4$ analysed in § 5.1 and a Newtonian fluid. Conversely, in an EVP filament with n varying from 0.4 to 0.6, analysed in §§ 5.5.1 and 5.5.2, χ_h exhibits a decreasing or constant trend, with a plateau at $O(10^{-2} - 10^{-4})$ as breakup is approached.
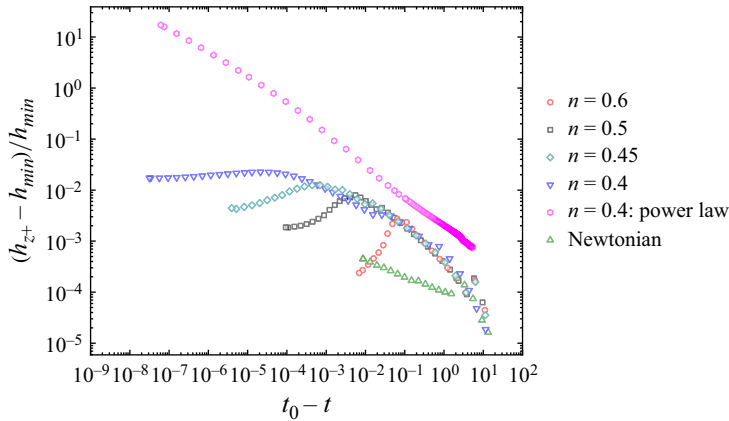
Figure 21. Evolution of $\chi_h = (h_{z^+} - h_{min})/h_{min}$ plotted against time to breakup $t_0 - t$ for EVP, power-law and Newtonian fluids. Other parameters for the EVP fluid are $Y_s = 0.1$, $Ec = 0.14$, $U = 0.1$, and those for the power-law fluid are provided in § 5.1. Here, $z^+ = 0.01$.

These observations suggest that the EVP filament retains an almost cylindrical shape very near pinch-off, consistent with finite-length breakup behaviour.

5.5.5. *Analysis of the local curvature at the symmetry plane*

In addition to analysing the scaling laws for minimum radius, axial stress or axial velocity at the interface on the symmetry plane $z = 0$, it is often important to examine the interfacial curvature and its asymptotic behaviour at this location. This becomes particularly relevant when it is important to distinguish between a SHB material with $n = 0.5$ and a Newtonian fluid, because both exhibit a similar linear decay of the minimum radius. As highlighted by Du *et al.* (2024), evaluation of the curvature at the mid-plane offers a more comprehensive characterisation of the filament shape than the decay of the minimum radius alone. Following this approach, we define the curvature ratio χ at the interface on the symmetry plane as

$$\chi = \frac{\kappa_z}{\kappa_r} = \frac{\left| \dfrac{h_{zz}}{\left(1 + h_z^2\right)^{\frac{3}{2}}} \right|}{\left| \dfrac{1}{h\left(1 + h_z^2\right)^{\frac{1}{2}}} \right|}. \tag{5.6}$$

Substituting (3.3) and (3.6) into the above expression yields a general asymptotic scaling form for χ

$$\chi \sim (t_0 - t)^{2\alpha_1 - 2\delta} \sim (h_{min})^{2 - \frac{2\delta}{\alpha_1}}. \tag{5.7}$$

Figure 22 shows the evolution of the curvature ratio, χ, as a function of the of minimum radius h_{min}, neglecting inertial effects. It includes SHB fluids in the range of exponents $n \in [0.4, 0.6]$, as well a power-law fluid with $n = 0.4$ and a Newtonian fluid.

According to Renardy (1994), the inertialess breakup asymptotic scaling exponents of a Newtonian fluid are $\alpha_1 = 1$ and $\delta = 0.175$, while for a power-law fluid with $n = 0.4$, they are $\alpha_1 = \delta = 0.4$, as discussed in § 5.1. Consequently, the asymptotic scaling of χ is expected to follow $(h_{min})^{1.65}$ for Newtonian fluid and remain constant for power-law
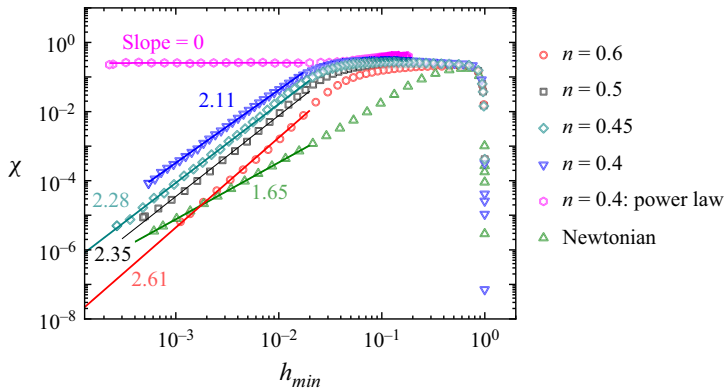
Figure 22. Evolution of the curvature ratio against minimum radius for EVP, power-law and Newtonian fluids. Other parameters for EVP fluid are $Y_s = 0.1$, $Ec = 0.14$, $U = 0.1$, and those for the power-law fluid are provided in § 5.1.

fluids under the assumption of negligible inertia. Notably, figure 22 reveals that the EVP fluid with $n = 0.5$ exhibits a numerically determined scaling exponent of approximately 2.35, which is significantly higher than that of the Newtonian case despite the fact that both fluids exhibit a similar linear decay in the minimum radius. This demonstrates that the evolution of the curvature ratio with respect to the minimum radius can effectively distinguish between the two cases, even though the formation of an elastic neck in the EVP fluids may not be fully observable in experiments. It is noteworthy that, having computed the curvature numerically, to evaluate curvature ratio χ, which involves the second derivative of the interface shape, we have calculated the ϕ_2 term in (3.18) as well. We opted not to report it explicitly for conciseness.

5.5.6. *Elasto-plasto-capillary regime with no breakup in finite time, $n = 1$*

Increasing n to unity to examine numerically the asymptotics of the Saramito–Bingham model, we revert to the asymptotes of the simpler Oldroyd-B fluids, which are known to predict that all variables and in particular the minimum radius have an exponential dependence on time to breakup. This is demonstrated in figure 23, where the minimum radius depends exponentially on time t, and the coefficient of the exponent is the same as the one for an Oldroyd-B fluid, $-1/(3 \times Ec \times \ln(10))$, while the coefficient of τ_{zz} has the opposite sign. The other two variables also have an exponential dependence on τ with the same coefficient between them, as required by the asymptotics. The final values of all variables required to cover the asymptotic range are much smaller now than in cases with $n < 1$, revealing that indeed the previous calculations are the most challenging ones. Once again, the YS plays no apparent role in the asymptotes.

6. Concluding remarks

In this study, we examined the dynamics of EVP filament breakup, while neglecting inertial effects as a first approach to understanding it. By utilising the SHB constitutive model, we derived the asymptotic behaviour and self-similar forms of the variables as the minimum filament radius approaches extremely small values. We show that the value of the YS is irrelevant when examining the late-stage asymptotic behaviour. Interestingly, we observed that the SHB model exhibits a similar asymptotic form as the G-PTT model,
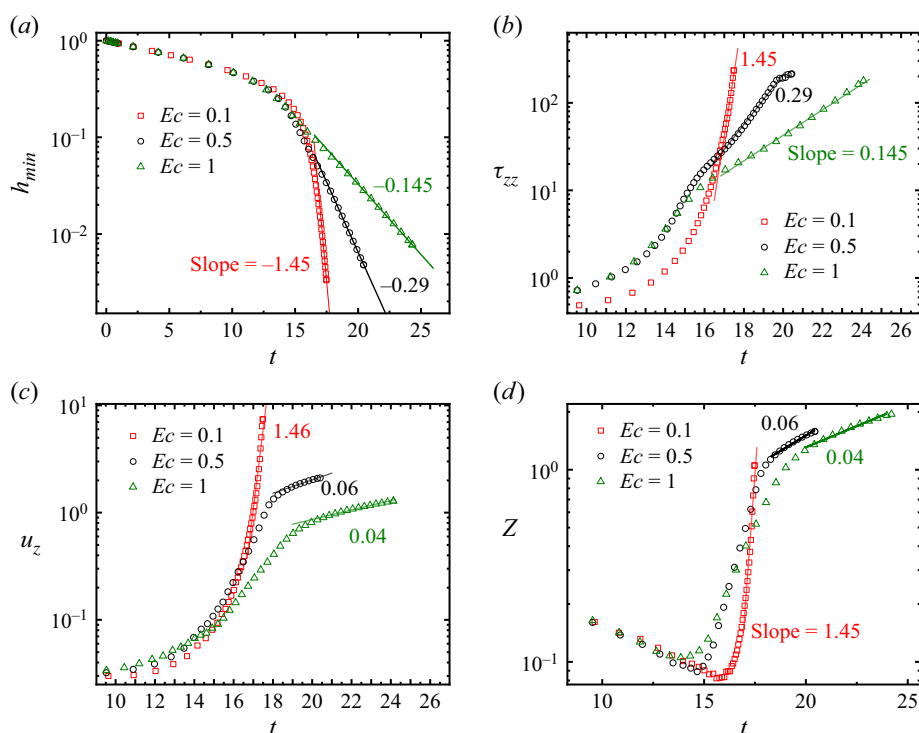
Figure 23. Effect of Ec on the scaling with respect to time (t) of minimum radius (a), axial stress (b), axial velocity (c) and axial length of neck (d). The rest of the parameters are $Y_s = 0.1$, $n = 1.$, $U = 0.1$.

previously analysed by Renardy, (2002a). We identified three distinct asymptotic regimes: (a) elasto-plasto-capillary and (b) elasto-plastic in both of which breakup takes place in finite time and (c) the elasto-plasto-capillary regime with no breakup in finite time. The former two cases arise when $n < 1$ and the latter when $n = 1$. We did not examine cases with $n > 1$, corresponding to shear-rate-thickening behaviour of the material. A comprehensive summary of the derived asymptotes is presented in table 4. By employing our recently developed numerical algorithm, PEGAFEM-V, we conducted 2-D axisymmetric simulations to capture the breakup process. To achieve minimum radius values as small as $O(10^{-4} - 10^{-5})$, we developed a novel stabilised adaptive finite element method capable of simulating any breakup scenario we encountered in this study. Using the 2-D simulation results, we derived self-similar solutions for the interface shape, axial velocity and axial stress by appropriately rescaling the variables, by scales presented in table 4.

We demonstrated that both the YS and the elasticity, represented by the coefficient of the upper-convected derivative in the constitutive equation, do not affect the determination of the asymptotic behaviour. The effect of Y_s is implicit for all examined n values, while the effect of Ec is implicit for $n < 1$, affecting only the intercept of the asymptotes and explicit for $n = 1$. We expect that other variants of Saramito's model, such as the Saramito–Giesekus model, will also exhibit the asymptotic behaviour of their viscoelastic counterpart during the late-stage breakup, as the YS becomes negligible in the dominant stress balance in the constitutive equation. We presented a scaling analysis that offers insights into experiments of extension of YS fluids with elastic properties, particularly where thixotropic effects are negligible. This analysis is very relevant to extensional rheology, where key quantities such as minimum filament radius or extensional viscosity are commonly reported.

	Finite time breakup $n < 1$		
	Extension-rate thinning $n < 0.5$ and constant extensional viscosity $n = 0.5$		
	Elasto-plastic breakup $0.33 < n < 0.43$	Elasto-plasto-capillary breakup $n \geq 0.43$	Extension-rate thickening $n > 0.5$	No breakup in finite time $n = 1$
h_{min}	$(t_o - t)^{\frac{n}{4-8n}}$	$(t_o - t)^{\frac{n}{1-n}}$	$(t_o - t)^{\frac{n}{1-n}}$	$e^{-\frac{t}{3Ec}}$
u_z	$(t_0 - t)^{\delta-1}$	$(t_0 - t)^{\delta-1}$	$(t_0 - t)^{\frac{n}{n-1}}$	e^{δ}
Z	$(t_0 - t)^{\delta}$	$(t_0 - t)^{\delta}$	$(t_0 - t)^{\frac{2n-1}{n-1}}$	e^{δ}
$|u_r|$	$(t_o - t)^{\frac{9n-4}{4-8n}}$	$(t_o - t)^{\frac{2n-1}{1-n}}$	$(t_o - t)^{\frac{2n-1}{1-n}}$	$e^{-\frac{t}{3Ec}}$
τ_{zz}	$(t_0 - t)^{\frac{n}{n-1}}$			$e^{\frac{t}{3Ec}}$
η_{ext}	$(t_0 - t)^{\frac{2n-1}{n-1}}$			$e^{\frac{t}{3Ec}}$
$\dot{\epsilon}$	$(t_0 - t)^{-1}$			Constant

Table 4. Summary of scales of all variables for breakup of an EVP filament when $Oh^{-2} = 0$.

We did not perform numerical simulations with the 1-D slender EVP filament. Following the findings of Moschopoulos *et al.* (2020) the slenderness of the filament may be influenced by the presence of YS, even though YS does not affect the late-time asymptotic behaviour. The final breakup shape and time might differ in 1-D slender simulations due to the YS affecting the filament's initial deformation up to the point very close to breakup. Future studies could explore the comparison between the results derived from 2-D and 1-D simulations across the full parameter space of YS and elasticity.

In future work, we will extend this study to provide a comprehensive understanding of EVP filament breakup including inertia. We will assess whether this leads to interfacial instabilities and the formation of bead-on-string structures in EVP filaments. Additionally, we plan to investigate the impact of thixotropy on breakup dynamics through full 2-D axisymmetric simulations of thixo-elasto-visco-plastic constitutive models, such as those developed by Spyridakis *et al.* (2024) and Varchanis *et al.* (2019a).

Author contributions. Pourya Zakeri: Software development and testing, Data curation, Investigation, Validation, Writing original draft. Pantelis Moschopoulos: Development of initial software, testing and validation, Yannis Dimakopoulos: Conceptualisation, Investigation, Methodology, Supervision, funding acquisition, Writing reviewing & editing. John Tsamopoulos: Conceptualisation, Investigation, Methodology, Validation, Supervision, Funding acquisition, Writing, reviewing & editing.
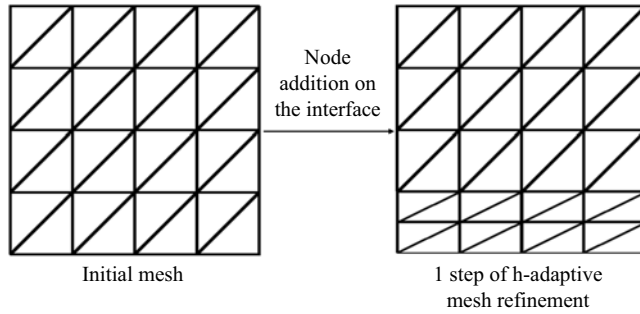
Figure 24. Schematic of h-adaptive mesh refinement. Nodes are added radially where any element exceeds the adaptation criteria.

Appendix A

A.1. *Mesh adaptation method*

The initial mesh is a unit square of side length 1. Concerning the elliptic grid generation scheme, the computational domain remains the unit square, and the physical domain deforms based on the imposed velocity on the top plate and the deformation of the free surface. The initial unit square is discretised into 500 axial elements and 30 radial elements leading to 15 000 nodes and 135 000 unknowns. As the filament stretches and the neck forms, the elements near and inside the neck will become skewed. To address this, we add nodes in the radial cross-section in the middle of every element in the computational domain if the minimum angle of the corresponding element in the physical domain falls below 25 degrees. Figure 24 shows schematically the h-adaptive mesh refinement after 1 step of node insertion. The mesh is shown in the computational domain for simplicity. However, adding nodes only based on the angle criterion may not be enough to have good accuracy of the solution. To address this, and motivated by our Petrov–Galerkin formulation, we define a characteristic pressure gradient for element k as follows:

$$\nabla p_k = \frac{\Sigma_{i=1}^{n_{en}} \left\| \nabla P_i^h \right\|}{n_{en}}, \tag{A1}$$

where n_{en} denotes the number of nodes in the element and $\|\nabla P_i^h\|$ is the L2-norm of the pressure gradient at each node. We use a pressure gradient-based error indicator defined as

$$\eta_k = \nabla p_k \cdot (\text{Area})_k. \tag{A2}$$

The error indicator η_k is normalised by the averaged error indication $\overline{\eta}_k$ over the domain

$$\overline{\eta}_k = \frac{\Sigma_{i=1}^{n_{el}} \eta_{k_i}}{n_{el}}. \tag{A3}$$

where n_{el} is the total number of elements. A node is added in the middle of every element if the ratio $(\eta_k/\overline{\eta}_k)$ exceeds 2. An additional criterion is developed by trial and error to prevent excessive node addition. Employing this error indicator results in less than 5 iterations per time step to reach the convergence criterion and achieve robust accuracy of the computed solution. Figure 25 depicts the adapted mesh just before breakup which contains more than 4×10^5 nodes and 3.6×10^6 unknowns.
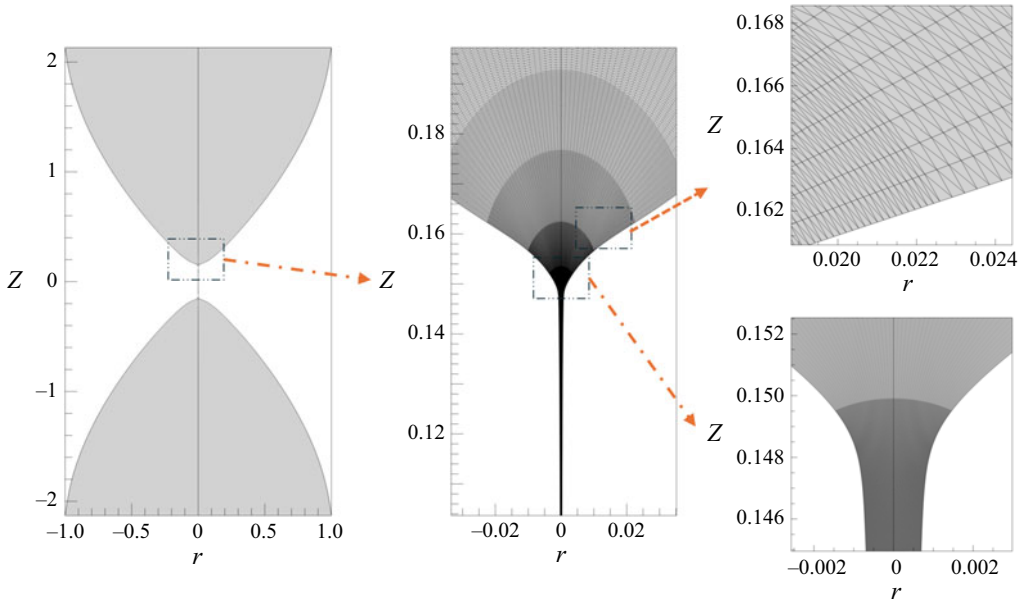
Figure 25. The adapted mesh with more than 400 000 nodes for the stretched filament; here $n = 0.45$, $Y_s = 1.25$, $EC = 0.14$ and $U = 0.39$.

A.2. *Solution transfer method*

After every adaptation step, values on the newly generated nodes must be computed. One straightforward method is to use the interpolants of the parent element to calculate these values. However, this method is not accurate enough, as we experienced in our calculations. This linear interpolation introduces inaccuracy, particularly in the pressure field, leading to spurious oscillations despite the use of a stabilised finite element method. Hence, to calculate the flow variables on the newly generated nodes, we use the conservative interpolation method introduced by Farrell & Maddison (2011). This method is a local L2-Galerkin projection which tries to minimise the L2 norm of a field between the old mesh and the new mesh by constructing a local supermesh. Supermesh is the mesh of the intersections of the new and the old mesh. For further details, the reader is referred to Farrell & Maddison (2011). The minimisation statement and the weak form of interpolation between the two meshes are as follows:

$$Minimize\ ||q_{old} - q_{new}||_2 \rightarrow \int_{\Omega_{new}} q_{new}\mathrm{d}\Omega = \int_{\Omega_{supermesh}} q_{old}\mathrm{d}\Omega. \tag{A4}$$

The integration on the left- and right-hand sides is conducted over the new mesh and the supermesh, respectively. This method ensures local conservation of integrals at the element level resulting in a smooth and continuous computed solution over time. The h-adaption method described here is straightforward, simple, and eliminates the need for the intersecting algorithm described in Farrell & Maddison (2011) to construct the supermesh. Figure 26 illustrates the supermesh constructed after one step of the h-adaptive mesh refinement. As the nodes of the old mesh, the new mesh and their local supermesh are predefined, implementing a code to generate the supermesh is both intuitive and computationally efficient.
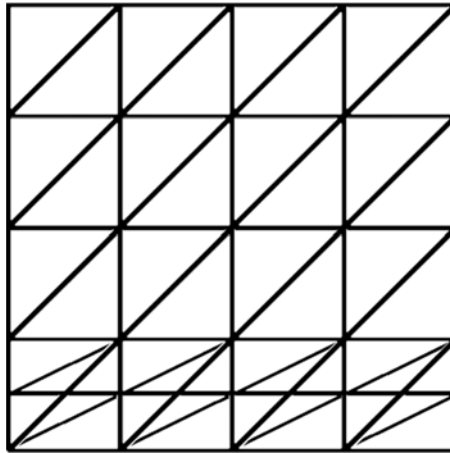
Figure 26. Constructed supermesh after one step of an h-adaptive mesh refinement.

REFERENCES

ANNA, S.L. & MCKINLEY, G.H. 2001 Elasto-capillary thinning and breakup of model elastic liquids. *J. Rheol.* **45** (1), 115–138.

ARNOLDS, O., BUGGISCH, H., SACHSENHEIMER, D. & WILLENBACHER, N. 2010 Capillary breakup extensional rheometry (CaBER) on semi-dilute and concentrated polyethyleneoxide (PEO) solutions. *Rheol. Acta* **49** (11), 1207–1217.

BALMFORTH, N.J., DUBASH, N. & SLIM, A.C. 2010a Extensional dynamics of viscoplastic filaments: i. Long-wave approximation and the Rayleigh instability. *J. Non-Newtonian Fluid Mech.* **165** (19–20), 1139–1146.

BALMFORTH, N.J., DUBASH, N. & SLIM, A.C. 2010b Extensional dynamics of viscoplastic filaments: II. Drips and bridges. *J. Non-Newtonian Fluid Mech.* **165** (19–20), 1147–1160.

BECHTEL, S.E., CAO, J.Z. & FOREST, M.G. 1992 Practical application of a higher order perturbation theory for slender viscoelastic jets and fibers. *J. Non-Newtonian Fluid Mech.* **41** (3), 201–273.

BHAT, P.P., APPATHURAI, S., HARRIS, M.T., PASQUALI, M., MCKINLEY, G.H. & BASARAN, O.A. 2010 Formation of beads-on-a-string structures during break-up of viscoelastic filaments. *Nat. Phys.* **6** (8), 625–631.

BRENNER, M.P., LISTER, J.R. & STONE, H.A. 1996 Pinching threads, singularities and the number 0.0304. *Phys. Fluids* **8** (11), 2827–2836.

CHAMBON, G., FREYDIER, P., NAAIM, M. & VILA, J.-P. 2020 Asymptotic expansion of the velocity field within the front of viscoplastic surges: comparison with experiments. *J. Fluid Mech.* **884**, A43.

CHATZIDAI, N., GIANNOUSAKIS, A., DIMAKOPOULOS, Y. & TSAMOPOULOS, J. 2009 On the elliptic mesh generation in domains containing multiple inclusions and undergoing large deformations. *J. Comput. Phys.* **228** (6), 1980–2011.

CHEN, A.U., NOTZ, P.K. & BASARAN, O.A. 2002 Computational and experimental analysis of pinch-off and scaling. *Phys. Rev. Lett.* **88** (17), 174501.

CLASEN, C., EGGERS, J., FONTELOS, M.A., LI, J. & MCKINLEY, G.H. 2006 The beads-on-string structure of viscoelastic threads. *J. Fluid Mech.* **556**, 283–308.

DEEN, W.M. 2012 *Analysis of Transport Phenomena*. 2nd edn. Oxford University Press.

DIMAKOPOULOS, Y. & TSAMOPOULOS, J. 2003 A quasi-elliptic transformation for moving boundary problems with large anisotropic deformations. *J. Comput. Phys.* **192** (2), 494–522.

DIMITRIOU, C.J. & MCKINLEY, G.H. 2014 A comprehensive constitutive law for waxy crude oil: a thixotropic yield stress fluid. *Soft Matt.* **10** (35), 6619–6644.

DOSHI, P., SURYO, R., YILDIRIM, O.E., MCKINLEY, G.H. & BASARAN, O.A. 2003 Scaling in pinch-off of generalized Newtonian fluids. *J. Non-Newtonian Fluid Mech.* **113** (1), 1–27.

DU, J., OHTANI, H., ELLWOOD, K. & MCKINLEY, G.H. 2024 Capillarity-driven thinning and breakup of weakly rate-thickening fluids. *J. Non-Newtonian Fluid Mech.* **331**, 105294.

EGGERS, J. 1993 Universal pinching of 3D axisymmetric free-surface flow. *Phys. Rev. Lett.* **71** (21), 3458.

EGGERS, J. & DUPONT, T.F. 1994 Drop formation in a one-dimensional approximation of the Navier–Stokes equation. *J. Fluid Mech.* **262**, 205–221.

EGGERS, J., HERRADA, M.A. & SNOEIJER, J.H. 2020 Self-similar breakup of polymeric threads as described by the Oldroyd-B model. *J. Fluid Mech.* **887**, A19.

ESPOSITO, G., DIMAKOPOULOS, Y. & TSAMOPOULOS, J. 2024 Buoyancy induced motion of a Newtonian drop in elastoviscoplastic materials. *J. Rheol.* **68** (5), 815–835.

FARRELL, P.E. & MADDISON, J.R. 2011 Conservative interpolation between volume meshes by local Galerkin projection. *Comput. Meth. Appl. Mech.* **200** (1–4), 89–100.

FONTELOS, M.A. & LI, J. 2004 On the evolution and rupture of filaments in Giesekus and FENE models. *J. Non-Newtonian Fluid Mech.* **118** (1), 1–16.

FRAGGEDAKIS, D., DIMAKOPOULOS, Y. & TSAMOPOULOS, J. 2016 Yielding the yield stress analysis: a thorough comparison of recently proposed elasto-visco-plastic (EVP) fluid models. *J. Non-Newtonian Fluid Mech.* **238**, 170–188.

FREYDIER, P., CHAMBON, G. & NAAIM, M. 2017 Experimental characterization of velocity fields within the front of viscoplastic surges down an incline. *J. Non-Newtonian Fluid Mech.* **240**, 56–69.

FRIGAARD, I. 2019 Simple yield stress fluids. *Curr. Opin. Colloid Interface Sci.* **43**, 80–93.

HOLENBERG, Y., LAVRENTEVA, O.M., SHAVIT, U. & NIR, A. 2012 Particle tracking velocimetry and particle image velocimetry study of the slow motion of rough and smooth solid spheres in a yield-stress fluid. *Phys. Rev. E - Stat. Nonlinear Soft Matt. Phys.* **86** (6), 066301.

HUISMAN, F.M., FRIEDMAN, S.R. & TABOREK, P. 2012 Pinch-off dynamics in foams, emulsions and suspensions. *Soft Matt.* **8** (25), 6767–6774.

KELLER, J.B. & MIKSIS, M.J. 1983 Surface tension driven flows. *SIAM J. Appl. Maths* **43** (2), 268–277.

KESHAVARZ, B., SHARMA, V., HOUZE, E.C., KOERNER, M.R., MOORE, J.R., COTTS, P.M., THRELFALL-HOLMES, P. & MCKINLEY, G.H. 2015 Studying the effects of elongational properties on atomization of weakly viscoelastic solutions using Rayleigh Ohnesorge Jetting Extensional Rheometry (ROJER). *J. Non-Newtonian Fluid Mech.* **222**, 171–189.

KORDALIS, A., DIMAKOPOULOS, Y. & TSAMOPOULOS, J. 2024 Hydrodynamic interaction between coaxially rising bubbles in elasto-visco-plastic materials: bubbles with a wide range of relative sizes. *Phys. Rev. Fluids* **9** (9), 093301.

KORDALIS, A., PEMA, D., ANDROULAKIS, S., DIMAKOPOULOS, Y. & TSAMOPOULOS, J. 2023 Hydrodynamic interaction between coaxially rising bubbles in elastoviscoplastic materials: equal bubbles. *Phys. Rev. Fluids* **8** (8), 083301.

KORDALIS, A., VARCHANIS, S., IOANNOU, G., DIMAKOPOULOS, Y. & TSAMOPOULOS, J. 2021 Investigation of the extensional properties of elasto-visco-plastic materials in cross-slot geometries. *J. Non-Newtonian Fluid Mech.* **296**, 104627.

LIU, Y., BALMFORTH, N.J., HORMOZI, S. & HEWITT, D.R. 2016 Two–dimensional viscoplastic dambreaks. *J. Non-Newtonian Fluid Mech.* **238**, 65–79.

LOPEZ, W.F., NACCACHE, M.F., DE, P.R. & MENDES, S. 2017 Rising bubbles in yield stress materials. *J. Rheol.* **62** (1), 209.

LUU, L.-H., PHILIPPE, P. & CHAMBON, G. 2017 Flow of a yield-stress fluid over a cavity: experimental study of the solid–fluid interface. *J. Non-Newtonian Fluid Mech.* **245**, 25–37.

MA, L. & BARBOSA-CHOVAS, G.V. 1995 Rheological characterization of mayonnaise. Part II: flow and viscoelastic properties at different oil and Xanthan gum concentrations. *J. Food Engng* **25** (3), 409–425.

MARTINIE, L., BUGGISCH, H. & WILLENBACHER, N. 2013 Apparent elongational yield stress of soft matter. *J. Rheol.* **57** (2), 627–646.

MCKINLEY, G.H. 2005 Visco-elasto-capillary thinning and break-up of complex fluids. *Annu. Rheol. Rev.*, https://dspace.mit.edu/handle/1721.1/18085.

MCKINLEY, G.H. & SRIDHAR, T. 2002 Filament-stretching rheometry of complex fluids. *Annu. Rev. Fluid Mech.* **34** (1), 375–415.

MOON, H., YAMANI, S., MCKINLEY, G.H. & LEE, J. 2024 Tuning the shear and extensional rheology of semi-flexible polyelectrolyte solutions, arXiv Preprint arXiv:2410.15132.

MOSCHOPOULOS, P., KOUNI, E., PSARAKI, K., DIMAKOPOULOS, Y. & TSAMOPOULOS, J. 2023 Dynamics of elastoviscoplastic filament stretching. *Soft Matt.* **19** (25), 4717–4736.

MOSCHOPOULOS, P., SPYRIDAKIS, A., DIMAKOPOULOS, Y. & TSAMOPOULOS, J. 2024 Unravelling the existence of asymmetric bubbles in viscoelastic fluids. *J. Fluid Mech.* **985**, A30.

MOSCHOPOULOS, P., SPYRIDAKIS, A., VARCHANIS, S., DIMAKOPOULOS, Y. & TSAMOPOULOS, J. 2021 The concept of elasto-visco-plasticity and its application to a bubble rising in yield stress fluids. *J. Non-Newtonian Fluid Mech.* **297**, 104670.

MOSCHOPOULOS, P., SYRAKOS, A., DIMAKOPOULOS, Y. & TSAMOPOULOS, J. 2020 Dynamics of viscoplastic filament stretching. *J. Non-Newtonian Fluid Mech.* **284**, 104371.

MOSCHOPOULOS, P., VARCHANIS, S., SYRAKOS, A., DIMAKOPOULOS, Y. & TSAMOPOULOS, J. 2022 S-PAL: a stabilized finite element formulation for computing viscoplastic flows. *J. Non-Newtonian Fluid Mech.* **309**, 104883.

MOUGIN, N., MAGNIN, A. & PIAU, J.M. 2012 The significant influence of internal stresses on the dynamics of bubbles in a yield stress fluid. *J. Non-Newtonian Fluid Mech.* **171–172**, 42–55.

NIEDZWIEDZ, K., ARNOLDS, O., WILLENBACHER, N. & BRUMMER, R. 2009 41969-1 how to characterize yield stress fluids with capillary breakup extensional rheometry (CaBER)? *Appl. Rheol.* **19** (4), 41969).

NIEDZWIEDZ, K., BUGGISCH, H. & WILLENBACHER, N. 2010 Extensional rheology of concentrated emulsions as probed by capillary breakup elongational rheometry (CaBER). *Rheol. Acta* **49** (11), 1103–1116.

NOTZ, P.K. & BASARAN, O.A. 2004 Dynamics and breakup of a contracting liquid filament. *J. Fluid Mech.* **512**, 223–256.

PAPAGEORGIOU, D.T. 1995 On the breakup of viscous liquid threads. *Phys. Fluids* **7** (7), 1529–1544.

PUTZ, A.M.V., BURGHELEA, T.I., FRIGAARD, I.A. & MARTINEZ, D.M. 2008 Settling of an isolated spherical particle in a yield stress shear thinning fluid. *Phys. Fluids* **20** (3), 033102.

RENARDY, M. 1994 Some comments on the surface-tension driven break-up (or the lack of it) of viscoelastic jets. *J. Non-Newtonian Fluid Mech.* **51** (1), 97–107.

RENARDY, M. 1995 A numerical study of the asymptotic evolution and breakup of Newtonian and viscoelastic jets. *J. Non-Newtonian Fluid Mech.* **59** (2–3), 267–282.

RENARDY, M. 2002*a* Self-similar jet breakup for a generalized PTT model. *J. Non-Newtonian Fluid Mech.* **103** (2–3), 261–269.

RENARDY, M. 2002*b* Similarity solutions for jet breakup for various models of viscoelastic fluids. *J. Non-Newtonian Fluid Mech.* **104** (1), 65–74.

RENARDY, M. & RENARDY, Y. 2004 Similarity solutions for breakup of jets of power law fluids. *J. Non-Newtonian Fluid Mech.* **122** (1–3), 303–312.

ROSELLO, M., SUR, S., BARBET, B. & ROTHSTEIN, J.P. 2019 Dripping-onto-substrate capillary breakup extensional rheometry of low-viscosity printing inks. *J. Non-Newtonian Fluid Mech.* **266**, 160–170.

SARAMITO, P. 2007 A new constitutive equation for elastoviscoplastic fluid flows. *J. Non-Newtonian Fluid Mech.* **145** (1), 1–14.

SARAMITO, P. 2009 A new elastoviscoplastic model based on the Herschel–Bulkley viscoplastic model. *J. Non-Newtonian Fluid Mech.* **158** (1–3), 154–161.

SPYRIDAKIS, A., MOSCHOPOULOS, P., VARCHANIS, S., DIMAKOPOULOS, Y. & TSAMOPOULOS, J. 2024 Thixo-elastoviscoplastic modeling of human blood. *J. Rheol.* **68** (1), 1–23.

SURYO, R. & BASARAN, O.A. 2006 Local dynamics during pinch-off of liquid threads of power law fluids: scaling analysis and self-similarity. *J. Non-Newtonian Fluid Mech.* **138** (2–3), 134–160.

TOWNSEND, J.M., BECK, E.C., GEHRKE, S.H., BERKLAND, C.J. & DETAMORE, M.S. 2019 Flow behavior prior to crosslinking: the need for precursor rheology for placement of hydrogels in medical applications and for 3D bioprinting. *Prog. Polym. Sci.* **91**, 126–140.

TULADHAR, T.R. & MACKLEY, M.R. 2008 Filament stretching rheometry and break-up behaviour of low viscosity polymer solutions and inkjet fluids. *J. Non-Newtonian Fluid Mech.* **148** (1–3), 97–108.

TURKOZ, E., LOPEZ-HERRERA, J.M., EGGERS, J., ARNOLD, C.B. & DEIKE, L. 2018 Axisymmetric simulation of viscoelastic filament thinning with the Oldroyd-B model. *J. Fluid Mech.* **851**, R2.

VAN DER KOLK, J., TIEMAN, D. & JALAAL, M. 2023 Viscoplastic lines: printing a single filament of yield stress material on a surface. *J. Fluid Mech.* **958**, A34.

VAN DER ZANDEN, J. & HULSEN, M. 1988 Mathematical and physical requirements for successful computations with viscoelastic fluid models. *J. Non-Newtonian Fluid Mech.* **29**, 93–117.

VARCHANIS, S., DIMAKOPOULOS, Y., WAGNER, C. & TSAMOPOULOS, J. 2018 How viscoelastic is human blood plasma? *Soft Matt.* **14** (21), 4238–4251.

VARCHANIS, S., HAWARD, S.J., HOPKINS, C.C., SYRAKOS, A., SHEN, A.Q., DIMAKOPOULOS, Y. & TSAMOPOULOS, J. 2020*a* Transition between solid and liquid state of yield-stress fluids under purely extensional deformations. *Proc. Natl Acad. Sci.* **117** (23), 12611–12617.

VARCHANIS, S., MAKRIGIORGOS, G., MOSCHOPOULOS, P., DIMAKOPOULOS, Y. & TSAMOPOULOS, J. 2019*a* Modeling the rheology of thixotropic elasto-visco-plastic materials. *J. Rheol.* **63** (4), 609–639.

VARCHANIS, S., PETTAS, D., DIMAKOPOULOS, Y. & TSAMOPOULOS, J. 2021 Origin of the Sharkskin instability: nonlinear dynamics. *Phys. Rev. Lett.* **127** (8), 088001.

VARCHANIS, S., SYRAKOS, A., DIMAKOPOULOS, Y. & TSAMOPOULOS, J. 2019*b* A new finite element formulation for viscoelastic flows: circumventing simultaneously the LBB condition and the high-Weissenberg number problem. *J. Non-Newtonian Fluid Mech.* **267**, 78–97.

VARCHANIS, S., SYRAKOS, A., DIMAKOPOULOS, Y. & TSAMOPOULOS, J. 2020*b* PEGAFEM-v: a new Petrov–Galerkin finite element method for free surface viscoelastic flows. *J. Non-Newtonian Fluid Mech.* **284**, 104365.

YILDIRIM, O.E. & BASARAN, O.A. 2001 Deformation and breakup of stretching bridges of newtonian and shear-thinning liquids: comparison of one-and two-dimensional models. In *Chemical Engineering Science*, vol. 56.

ZHANG, X., PADGETT, R.S. & BASARAN, O.A. 1996 Nonlinear deformation and breakup of stretching liquid bridges. *J. Fluid Mech.* **329**, 207–245.